



Universiteit
Leiden
The Netherlands

Data combination: interferometry and single-dish imaging in radio astronomy

Plunkett, A.; Hacar Gonzalez, A.; Moser-Fischer, L.; Petry, D.; Teuben, P.; Pingel, N.; ... ; Mason, B.

Citation

Plunkett, A., Hacar Gonzalez, A., Moser-Fischer, L., Petry, D., Teuben, P., Pingel, N., ... ; Mason, B. (2023). Data combination: interferometry and single-dish imaging in radio astronomy. *Publications Of The Asp*, 135(1045). doi:10.1088/1538-3873/acb9bd

Version: Publisher's Version
License: [Creative Commons CC BY 4.0 license](#)
Downloaded from: <https://hdl.handle.net/1887/3719034>

Note: To cite this publication please use the final published version (if applicable).



Data Combination: Interferometry and Single-dish Imaging in Radio Astronomy

Adele Plunkett¹ , Alvaro Hacar^{2,3} , Lydia Moser-Fischer⁴, Dirk Petry⁵ , Peter Teuben⁶ , Nickolas Pingel^{7,8} ,
Devaky Kunneriath¹ , Toshinobu Takagi⁹, Yusuke Miyamoto^{10,11} , Emily Moravec¹² , Sümeyye Suri² ,
Kelley M. Hess^{13,14} , Melissa Hoffman¹⁵ , and Brian Mason¹

¹ National Radio Astronomy Observatory, 520 Edgemont Road, Charlottesville, VA 22903, USA; aplunket@nrao.edu

² Department of Astrophysics, University of Vienna, Türkenschanzstrasse 17, 1180, Vienna, Austria

³ Leiden Observatory, Leiden University, PO Box 9513, 2300-RA Leiden, The Netherlands

⁴ Argelander-Institut fuer Astronomie, Auf dem Huegel 71, D-53121 Bonn, Germany

⁵ European Southern Observatory, Karl-Schwarzschild-Strasse 2, D-85748 Garching, Germany

⁶ Astronomy Department, University of Maryland, 4296 Stadium Drive, College Park, MD 20742, USA

⁷ Department of Astronomy, University of Wisconsin–Madison, 475 North Charter Street, Madison, WI 53706, USA

⁸ Research School of Astronomy and Astrophysics, The Australian National University, Canberra, ACT 2611, Australia

⁹ Japan Space Forum, 3-2-1 Kandasurugadai, Chiyoda-ku, Tokyo 101-0062, Japan

¹⁰ Department of Electrical and Electronic Engineering, Fukui University of Technology, 3-6-1, Gakuen, Fukui, 910-8505, Japan

¹¹ National Astronomical Observatory of Japan, 2-21-1 Osawa, Mitaka, Tokyo 181-8588, Japan

¹² Green Bank Observatory, PO Box 2, Green Bank, WV 24944, USA

¹³ Instituto de Astrofísica de Andalucía (CSIC), Glorieta de la Astronomía s/n, E-18008 Granada, Spain

¹⁴ ASTRON, The Netherlands Institute for Radio Astronomy, Postbus 2, 7990 AA, Dwingeloo, The Netherlands

¹⁵ Space Telescope Science Institute, 3700 San Martin Drive, Baltimore, MD 21218, USA

Received 2022 December 3; accepted 2023 February 7; published 2023 March 20

Abstract

Modern interferometers routinely provide radio-astronomical images down to subarcsecond resolution. However, interferometers filter out spatial scales larger than those sampled by the shortest baselines, which affects the measurement of both spatial and spectral features. Complementary single-dish data are vital for recovering the true flux distribution of spatially resolved astronomical sources with such extended emission. In this work, we provide an overview of the prominent available methods to combine single-dish and interferometric observations. We test each of these methods in the framework of the CASA data analysis software package on both synthetic continuum and observed spectral data sets. We develop a set of new assessment tools that are generally applicable to all radio-astronomical cases of data combination. Applying these new assessment diagnostics, we evaluate the methods' performance and demonstrate the significant improvement of the combined results in comparison to purely interferometric reductions. We provide combination and assessment scripts as add-on material. Our results highlight the advantage of using data combination to ensure high-quality science images of spatially resolved objects.

Unified Astronomy Thesaurus concepts: [Millimeter astronomy \(1061\)](#); [Submillimeter astronomy \(1647\)](#); [Interferometry \(808\)](#); [Fast Fourier transform \(1958\)](#); [Spectroscopy \(1558\)](#); [Astronomical techniques \(1684\)](#)

Online material: color figures

1. Introduction

A well-known challenge of interferometric imaging in the radio and submillimeter regimes is that it relies on aperture synthesis in which the Fourier or (u, v) plane is irregularly or incompletely sampled. While interferometry is a powerful technique for resolving structures on smaller scales than can be attained with a single-dish (SD) telescope, on the other hand,

an SD telescope is necessary for recovering extended structure. This is commonly known as the “short-spacing” problem that we show in Figure 1, visualized as a “hole” in the inner region of the (u, v) coverage (e.g., Wilner & Welch 1994; Kurono et al. 2009); visualizations in the literature are given by Mason (2020; see their Section 2.2 and Figures 2–4) and Leroy et al. (2021; Figures 24–25), among others. The lack of short spacings in the interferometer results in the inability to detect the flux of large spatial scales and thus leads to an incomplete representation of the true sky brightness distribution in the image. Ideally, observations would sample the complete (u, v) space corresponding to the spatial scales under study and

Original content from this work may be used under the terms of the [Creative Commons Attribution 3.0 licence](#). Any further distribution of this work must maintain attribution to the author(s) and the title of the work, journal citation and DOI.

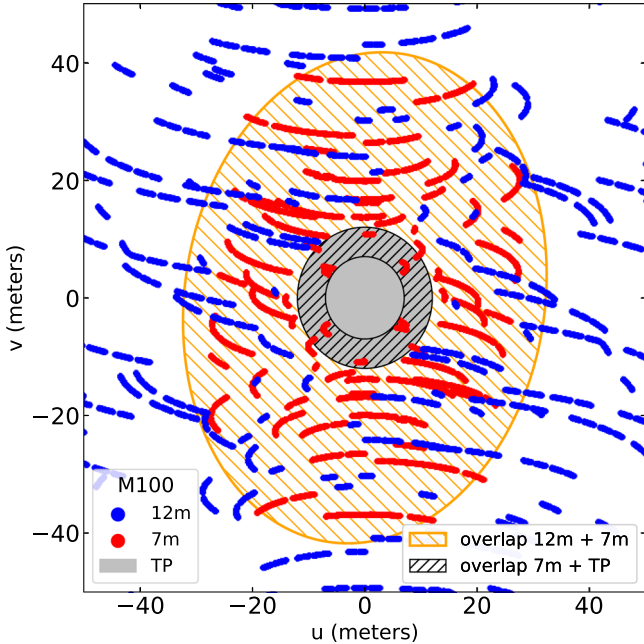


Figure 1. Central (u, v) coverage of the M100 data set presented in this work showing all baselines of ≤ 50 m observed by the 12 m (blue), 7 m (red), and TP (gray) arrays. Different ellipses highlight the overlapping (u, v) coverage between the 12 and 7 m (hatched orange area) and between the 7 m and TP (hatched black area) arrays. Significant overlap between different arrays is preferred for data combination.

recover consistent amplitudes at overlapping (u, v) distances if multiple interferometry configurations and SD observations are required (see, e.g., Figure 3 of Koda et al. 2019). As described in Rau & Cornwell (2011), the impact of the zero-spacing problem is not restricted to continuum images. Spectra can also be strongly affected, as shown in molecular line observations (e.g., Pety et al. 2013; Hacar et al. 2018; see also Section 6.2).

The solution is to complement the interferometric observations with a separate observation with an instrument sensitive to the large scales, typically an SD telescope, using data combination. For example, in the case of the Atacama Large Millimeter/submillimeter Array (ALMA), this is done by combining data from the main ALMA 12 m array and/or the ALMA 7 m Compact Array (ACA) with data from the dedicated ALMA SD (or total power, TP) telescopes. A broad literature highlights the critical role of data combination in both Galactic and extragalactic studies, including a large variety of interferometer-plus-SD combinations not only within ALMA (for a very thorough example, see Leroy et al. 2021, among others) but also using the CARMA and NRO 45 m/IRAM 30 m/FCRAO (Koda et al. 2011; Plunkett et al. 2013, 2015; Kong et al. 2018), SMA and APEX (Kauffmann et al. 2017), (E)JVLA and GBT (Pineda et al. 2011; Williams et al. 2018; Wang et al. 2020), PdBI/NOEMA and IRAM 30 m (Pety et al. 2013; Beuther et al. 2022), ALMA 12 m and MOPRA/IRAM

30 m (Peretto et al. 2013; Hacar et al. 2018), or ASKAP and Parkes (Pingel et al. 2022) telescopes, to cite some examples.

Interferometric image synthesis and data combination is not a new topic. Stanimirovic (2002) provided a comprehensive introduction to the problem and the history of solution attempts. An update was given by Mason (2020) concentrating on the “feathering” technique of data combination. Most generally, methods exist for combination at different steps of the imaging process, either in the spatial frequency (Fourier) domain or in the image domain. However, a systematic and quantitative comparison of the results of these methods is still missing.

In this work, we summarize current data combination techniques and provide new tools to evaluate their performance. After setting the foundation by briefly describing important aspects of imaging purely interferometric data in Section 2, we present the prominent existing methods for combining interferometric and SD observations in Section 3. In Section 4, we specify a simulated and an observed test data set for our evaluation of methods. In Section 5, we describe in detail our new assessment metrics for interferometric and combined images, which are implemented in our new performance evaluation tools. We then run the described combination methods on the test data sets and evaluate the results. Finally, in Section 6, we derive general recommendations for the use of the combination methods. The script suite for running the combination methods and our evaluation tools and the data to reproduce the figures in this paper are available from <https://github.com/teuben/DataComb>.

2. Imaging Interferometric Data with CLEAN

There is a Fourier transform (FT) relationship between the signals from the antennas making up an interferometer and the sky brightness distribution. The correlated signals, known as visibilities, are visualized in the (u, v) plane, and an inverse FT is used to provide an image of the spatial plane (see Mason 2020). The point-spread function (PSF) of the interferometer is the FT of the visibilities, and as these do not fill the (u, v) plane, the PSF can be highly irregular. An initial step of imaging produces the so-called “dirty” image, which is the convolution of this PSF with the true sky brightness distribution. The PSF side lobes manifest as image artifacts. Thus, subsequent deconvolution is necessary to optimize image quality. Presently, the most commonly used deconvolution algorithms are based on CLEAN (Högbom 1974; Clark 1980).

CLEAN deconvolves the data from the effects of the PSF of the interferometer by iteratively modeling the emission as a set of point sources (delta functions). The final image and residuals are convolved with an idealized restoring beam based on the FWHM of the PSF. CLEAN achieves good image quality for astronomical objects comparable in size to the angular

resolution. For objects significantly larger, typically multiscale CLEAN (Cornwell 2008) is used, which employs inverted truncated paraboloids instead of delta functions to model the emission. CLEAN algorithms also incorporate options for weighting visibilities and interpolating into the missing spacings in the (u, v) plane, which provide a trade-off between resolution and sensitivity but can themselves introduce artifacts if the sky brightness has structure on the unsampled scales such that the interpolation is inaccurate. Further extensions of CLEAN (MT-MFS CLEAN; Rau & Cornwell 2011) account for the frequency dependence of the (u, v) coverage.

For the actual data analysis work in this study, we exclusively use the Common Astronomy Software Applications (CASA) package (The CASA Team et al. 2022) version 6.1. CASA is the primary data analysis package for ALMA and the Karl G. Jansky Very Large Array (VLA). Other available radio-astronomical data analysis packages include AIPS (van Moorsel et al. 1996), GILDAS (Pety 2005; Gildas 2013), and MIRIAD (Sault et al. 1995) and more recently developed programs such as `wsclean` (Offringa et al. 2014), `resolve` (Arras et al. 2021), and `purify` (Carrillo et al. 2014).

In CASA, CLEAN and its extensions are all accessible via the `tclean` task. Additionally, all of the data combination methods presented in Section 3 can be implemented by calling CASA tasks. Some are already available as a single CASA task (such as `sdintimaging` and `feather`) or add-on packages for CASA (`tp2vis`). Each method in Section 3 uses `tclean` (or the underlying libraries of `tclean`) at some step in the imaging and data combination process.

The user can control the behavior of `tclean` via a large set of input parameters that are explained in the CASA documentation.¹⁶ Some of the most critical parameters are those related to (a) the number of deconvolution iterations, (b) the CLEAN threshold (i.e., the minimum flux justifying the placement of a CLEAN component), (c) the spatial masking (where the CLEAN components can be placed), and (d) the handling of the relative weighting of the interferometric visibilities.

To facilitate the comparison among the combination methods, we fix all `tclean` parameters to common values. We set the number of iterations to 100,000. We use Briggs weighting (Briggs 1995) with a robust value of 0.5 (i.e., balance between natural and uniform weighting) for all runs of `tclean`, as well as `gridder='mosaic'`; in this study, we deal exclusively with 'mosaic' maps, but `gridder='mosaic'` applies for the case of combining data from multiple arrays of different antenna sizes, even if they are single-pointing observations.

We explored several masking options, as careful masking is important to mitigate constructive interference of the side lobes of the synthesized beam (Condon et al. 1998). The mask is

generated by first utilizing the SD image to mask (include) all regions above 0.3 times the maximum value in the SD image and in the next step include any additional regions selected by the “auto-multithresh” algorithm in `tclean` (Kepley et al. 2020) using the standard “auto-multithresh” parameters. This masking technique is determined to capture the regions of larger-scale emission (as in the SD image), as well as any regions of more compact emission that might appear primarily in the interferometry data. Finally, the spectral definition mode can be chosen to be either “mfs” (multifrequency synthesis, for continuum imaging with only one output image channel) or “cube” (for spectral line imaging with one or more channels), depending on the data set and desired image. In this paper, we present continuum and spectral data as an image and a cube, respectively.

3. Combination Methods

In this section, we describe the theory and execution of the currently available data combination methods we have selected for evaluation in this study (see also Table 1). The methods incorporate one or more of the following steps in order to combine the interferometry data set(s) with SD observations: combine the SD data with a clean interferometer image; combine the SD data with a dirty interferometer image before joint deconvolution; and convert the SD data to pseudovisibilities, combine in the (u, v) plane, and then FT the combined data and CLEAN. The methods we present for evaluation are Feather (Section 3.1), SDINT (Section 3.2), model-assisted CLEAN plus Feather (MACF; Section 3.3), Total Power Map to Visibilities (TP2VIS; Section 3.4), and Faridani et al.’s (2018) short-spacing correction (FSSC; Section 3.5). For each of these methods, we include a list of the control parameters.

We note that the prerequisites common to all combination methods presented here are the following.

1. All data have been fully calibrated (this would also include the possibility of self-calibration, if applicable).
2. Astrometry should align.
3. Images have overlapping, well-sampled spatial frequencies, i.e., adequate coverage of the (u, v) plane among combined data sets.
4. Images have well-defined beams: the primary beam (PB) of the low-resolution image, $PB_{\text{low-res}}$, and the PB of the high-resolution image, $PB_{\text{hi-res}}$.
5. The bandwidth is narrow enough that the frequency-dependent scaling of the baseline lengths and the PB can be ignored, although SDINT can in fact take this into account.

We assume that the flux scales are aligned, but further fine-tuning can be done for specific use cases. Generally, every input image is assumed to be corrected for all instrumental effects, including PB response. We refer to the documentation

¹⁶ <https://casadocs.readthedocs.io/>

Table 1
Summary of Data Combination Methods

Methodology ^a	Domain ^b	Method	Task Name	Input		Output
				Interferometry	SD	
Before	F/I	SDINT	sdintimaging	Vis.	Image	Image
	F	TP2VIS	tp2vis ^c tclean	Vis. Vis.	SD image Pseudovisibilities	Pseudovisibilities Image
During	F + I	MACF	tclean	Vis.	Image as model	Image
			feather	Image	Image	Image
After	F	Feather	feather	Image	Image	Image
	I	FSSC	(script)	Image	Image	Image

Notes.

^a Indicates combination before, during, or after image deconvolution.

^b Fourier (“F”) or image (“I”) domain in which the method operates.

^c Only available in CASA after importation of the TP2VIS package.

of each method (i.e., CASA Guides, Github, etc.) for guidance on handling units and the specific treatments of the PB response during the respective steps of the data combination (sometimes referred to as DC) process. Finally, we use test cases without bright emission that extends or emerges beyond the area of the well-characterized PB response. The same methods should, in principle, be adaptable to other scenarios.

3.1. Feather

3.1.1. Feather Algorithm

The Feather algorithm is probably the most well-known method for combining SD and interferometric data. The algorithm is implemented as a CASA task of the same name. This method inverts the input images via FT and combines them in Fourier space (i.e., the (u, v) plane), weighting them according to the spatial frequencies of the response of each telescope. The combined data are then FTed back to the image plane.

Although `feather` does regrid, in some cases, regridding may be better to do outside the task, in which case, `imregrid` and `specsmooth` can be used. For a more comprehensive discussion of Feather, see Cotton (2017); the CASA documentation fully explains the additional parameters.¹⁷

¹⁷ An alternative implementation of the Feather algorithm is possible with the `uvcombine` package in Python, which implements a similar approach to CASA’s `feather` task but with additional options. See <https://github.com/radio-astro-tools/uvcombine>. In Miriad, `immerge` offers the option `feather`, allowing the combination of two images with Gaussian PSFs (see <https://github.com/baobabyoo/almica> for implementation). Additionally, `J-comb` (Jiao et al. 2022) is a new linear combination technique that has been benchmarked against both CASA’s `feather` and Miriad’s `immerge` tasks but is not further explored in this work. See Jiao et al. (2022) for additional information about their investigation into the `feather` and `immerge` implementations.

In more detail, the step-by-step order of operations undertaken with the `feather` task can be enumerated by the following.

1. Regrids the SD/low-resolution image spatially and spectrally to the high-resolution image.
2. FTs both images, such that the next steps operate on the visibilities.
3. Scales the FT low-resolution image by the ratio of clean beams (CBs),

$$CB_{\text{hi-res}}/CB_{\text{low-res}}, \quad (1)$$

in order to account for different beam sizes.

4. Adds the FT of the high-resolution image $\times(1 - \omega t)$ to the scaled FTed low-resolution image, where ωt is the FT of $CB_{\text{low-res}}$. In other words, the images have been weighted and combined in the (u, v) plane.
5. FTs back to the imaging plane.

3.1.2. Feather Parameters

From the CASA documentation, the `feather` command inputs include those listed in Table 2. Two particularly important parameters to consider for `feather` are `sdfactor` and `effdishdiam`. Here `sdfactor` is used to adjust the flux scale of the SD image. It should be constrained by comparing flux where there is overlap between the spatial frequencies in the low- and high-resolution images, and empirically, the value is most commonly set close to 1.0–1.2. The parameter `sdfactor` has parallels to `sdgain` in `sdintimaging` in SDINT (see Section 3.2), but they are not mathematically identical. Here `effdishdiam` is the effective diameter of the SD telescope, corresponding to the “low-res” image in the `feather` command; the effective dish

Table 2
Parameters for Feather Method

CASA Task	Parameter	Default	Description
feather	imagename	=""	Name of output feathered image
	highres	=""	Name of high-resolution (interferometer) image
	lowres	=""	Name of low-resolution (SD) image
	sdfactor	=1.0	Scale factor to apply to SD image
	effdishdiam	=-1.0	Effective diameter (in meters) of the SD telescope
	lowpassfiltersd	=False	Filter out the high spatial frequencies of the SD image

diameter depends on the aperture efficiency and is generally determined/reported for a given telescope. When Feathering, the weighting function for the SD data is usually the FT of the SD PB (PB_{SD}), but the weighting function can be altered by indicating a reduced SD diameter, corresponding to a different PB_{SD} . We did not further investigate the impact of `lowpassfiltersd`.

3.2. Joint Deconvolution: SDINT

3.2.1. The SDINT Algorithm

The SDINT algorithm (Rau et al. 2019) permits joint deconvolution of wideband SD and interferometer data and has been implemented as the task `sdintimaging` in CASA.¹⁸ We refer the reader to Rau et al. (2019) for full details and explanatory diagrams, and we briefly describe the algorithm here. The main inputs to the algorithm are the SD image and PSF (as a cube, if applicable), as well as the interferometric data set. Note that if no SD PSF is provided, `sdintimaging` can solve for the beam information based on the image header.

The `sdintimaging` algorithm follows these steps.

1. The process starts as for standard ‘‘CLEANing’’ with a ‘‘major cycle’’ in which the interferometric data are gridded and FTed into an image cube. At the same time, the corresponding PSF is formed.
2. Then, the SD cube is combined with the interferometric cube in a Feathering step (see Section 3.1).
3. A similar combination is applied to the interferometric PSF and the representative SD kernel to form a joint PSF. The joint image and PSF cubes then form inputs to a standard CLEAN ‘‘minor cycle’’ deconvolution.
4. As the minor cycle limits are reached, model images from the deconvolution are translated back (depending on the chosen deconvolution algorithm) to model image cubes that are then (a) subtracted from the SD image cube to form a new residual SD image and (b) FTed and degridded to form a new set of residual interferometric visibilities.

5. These visibilities, together with the residual SD image, then form the input to the next major cycle and Feathering. For mosaicking, appropriate application of the PB correction takes place prior to deconvolution.

Because it is based on the standard CLEAN family of algorithms, the task `sdintimaging` shares many parameters with the task `tclean` in CASA, as well as controls for a Feathering step to combine interferometer and SD data sets within the imaging iterations. The most important parameter to control the Feathering step is `sdgain`. This parameter decides on the relative weight of interferometric and SD data, similar to the relative weight for the visibilities from different baselines in pure interferometric imaging. The default setting for `sdgain` is 1.0, i.e., equal weight to both contributions. A value smaller than 1.0 will give the SD contribution less weight than the interferometric one, while a value greater than 1.0 gives it more weight. The flux scale of the joint image, however, will be kept constant. The best way to understand the role of `sdgain` is to think of the combination as forming a weighted mean of two measurements. In standard error propagation, the relative weight of different measurements of the same quantity should be

$$w_i = \frac{\sigma_i^{-2}}{\sum_j \sigma_j^{-2}}, \quad (2)$$

where w_i is the weight, and σ_i is the error on the i th measurement. The natural `sdgain` value is thus a function of the noise or sensitivity of the SD and the interferometric contributions and should be close to 1.0 if the sensitivities are similar, larger than 1.0 if the SD observation is more sensitive, and smaller than 1.0 if it is less sensitive than the interferometric one.

3.2.2. SDINT Parameters

Here we specify parameters specifically applicable when `usedata='sdint'`, which is the case we explore for combination in this work. Here `dishdia` should be considered as the effective dish diameter of the SD, and if `sdpsf` is given as a dish diameter, this parameter will be ignored. For a summary of pertinent parameters, see Table 3.

¹⁸ The task `sdintimaging` is incorporated in CASA 5.7/6.1 and subsequent releases.

Table 3
Parameters of SDINT Method

CASA Task	Parameter	Default	Description
sdintimaging	usedata	“sdint”	Output image type (int, sd, sdint)
	vis	“”	Input interferometric visibility data
	sdimage	“”	Input SD image
	sdpsf	“”	Input SD PSF image
	sdgain	1.0	Factor or gain to adjust SD flux scale
	dishdia	100.0	SD diameter (in meters)
	selectdata	“”	Enable data selection parameters, as in <code>tclean</code>

3.3. Model-assisted CLEAN plus Feather Method

There is another method that is, in essence, a variant of `feather`, and we refer to it as the MACF (for a list of the input parameters, see Table 4). It utilizes `feather` to ultimately combine the interferometric and SD images (as in Section 3.1) but takes a slightly different approach to generate the interferometric image used as input. The parameter `startmodel` is used when invoking `tclean` on the interferometric data, providing the SD image (in units of Janskys per pixel) as the starting model image.¹⁹

The advantage of cleaning with the SD image as a starting model is that the extended emission is conveyed in the model image, and then interferometer-based clean components are incorporated before convolving with a CB for the final image restoration (adding residuals). A caveat is that the zero-spacing flux, although initialized, is not constrained by `tclean`, so this should be considered an intermediate image only.

The next step is to combine this interferometry-with-startmodel image with the SD image using `feather`. This step in the combination procedure is identical to that described in Section 3.1. Examples of the application of the MACF method to observations can be found in Dirienzo et al. (2015), Kauffmann et al. (2017), and Hacar et al. (2018).

3.4. TP2VIS

The package TP2VIS²⁰ was developed for joint deconvolution of ALMA 12 m, 7 m, and TP data and is thoroughly presented by Koda et al. (2019). We reiterate that TP is another name used by radio astronomers for SD data. The TP2VIS package operates in CASA to convert an SD map into visibilities; these so-called “pseudovisibilities” can then be used as input for joint deconvolution along with interferometric visibilities. The technique has been presented and utilized by several authors (e.g., Rodríguez-Fernández et al. 2008; Kurono et al. 2009; Pety & Rodríguez-Fernández 2010; Koda et al.

¹⁹ A similar procedure to our MACF is documented by J. Kauffmann and available at <http://tinyurl.com/zero-spacing>.

²⁰ The TP2VIS package is available via Github at <https://github.com/tp2vis/distribute>.

Table 4
Parameters for MACF Method

CASA Task	Parameter	Default	Description
<code>tclean</code>	<code>startmodel</code>	=“”	Name of low-resolution (SD) image
<code>feather</code>	<code>imagenname</code>	=“”	Name of output feathered image
	<code>highres</code>	=“”	Name of high-resolution (interferometer) image generated after using low-resolution image as “startmodel”
	<code>lowres</code>	=“”	Name of low-resolution (SD) image

2011, and references therein), with the TP2VIS package being the first and only implementation in CASA.

The TP2VIS package is roughly structured in four steps, with much more detail on each available in Koda et al. (2019).

1. The SD map is converted into the sky brightness distribution, to be observed as if by a virtual interferometer.
2. The `tp2vis` function converts the brightness distribution into visibilities.
3. Next, there is an option to set the weights of the TP visibilities according to a few weighting schemes, such as that they represent the rms noise of the original TP map or are set to a constant value.
4. Finally, combination is done by deconvolving the pseudovisibilities and interferometric visibilities jointly using the `tclean` task.

The TP2VIS package also offers the function `tp2vistweak`, which attempts to fix the problem of discrepant beam sizes of the dirty beams and CBs in the image space after deconvolution, as detailed in Jorsater & van Moorsel (1995).

In our tests with CASA 6,²¹ TP2VIS turned out to be less straightforward to use effectively and consistently across different data sets compared with the other combination methods described here. In order not to further delay the publication, we decided not to include it in the evaluation

²¹ We note that TP2VIS was developed with an earlier version of CASA, as reported by Koda et al. (2019).

section of this paper. We have, however, included it in the accompanying software (Section 3.6).

3.5. FSSC method

Implementations that utilize fast Fourier transforms (FFTs), such as the Feather method, may introduce artifacts into the final combined image due to structures that extend up to or beyond the edge of the image, creating a sharp discontinuity. This is the case for the `feather` task. Faridani et al. (2018) introduced a combination method that works purely in the image domain to avoid the introduction of such artifacts; they provide a stand-alone Python code that we have also incorporated into our suite of combination methods in order for the implementation to be done consistently. The method is succinctly summarized in Equation (6) of Faridani et al. (2018):

$$\begin{aligned} I_{\text{missing}} &= I_{\text{sd}}^{\text{reg}} - I_{\text{int}}^{\text{conv}} \\ I_{\text{comb}} &= I_{\text{int}} + \alpha \cdot I_{\text{missing}}. \end{aligned} \quad (3)$$

The missing flux (I_{missing}) of the interferometry observations is determined by first taking the difference between the SD image at its native resolution, $I_{\text{sd}}^{\text{reg}}$, and the interferometer-only image that has been convolved and regridded to the angular resolution and pixel scale of the SD image, $I_{\text{int}}^{\text{conv}}$. The combined image is then the sum of the original interferometer-only image I_{int} and this missing flux image, also scaled by α , which is the ratio of the clean interferometer beam to the SD beam, to account for the difference in beam sizes (Equation (1)). In addition to mitigating potential FFT artifacts, this approach is also less computationally expensive, since no FFTs are required. Similar to `feather`, an additional scaling factor can be applied to the SD image to compensate for differences in the flux scale beyond the differences in beam sizes.

We refer to this process as the FSSC method and note that the output images are very similar to those from the Feather technique. While the concepts are equivalent, the FSSC method operates purely in the image plane, with no FTs, contrary to Feather. This technique has successfully been used to combine images from the Large Millimeter Telescope, Planck, and the Caltech Submillimeter Observatory to create a 1.1 mm image of the Central Molecular Zone of our Galaxy sensitive to all angular scales down to $10''5$ (Tang et al. 2021a, 2021b).

3.6. Software Developed in This Study

In this work, we provide a single data combination script (called “DC_script” that runs with Python and incorporates Astropy; Astropy Collaboration et al. 2018) that performs (a) the data combination methods described in Section 3 on simulated and observational data sets (Sections 4.1 and 4.2) and (b) the assessment methods described in Section 5. The script, data, and documentation are available at <https://github.com/teuben/DataComb>. When running the script for the first

time, follow the steps in the README file. Also available in the code repository are an overview of all steps, a “quick start” guide, and template parameter files. The “DC_script” is optimized to run noninteractively, but the user can choose to run interactively if needed in order to change certain parameters. It also includes the full set of quality assessment metrics described in this work to evaluate the performance of the different data combination methods (Section 5).

4. Test Data Sets

4.1. Simulated Continuum Observations

Only with simulated observations can the accuracy of the image reconstruction be properly measured, since in that case, the “true” intensity distribution on the sky is known. For efficiency, we try to capture a large range of possible source structures in a single test image to study. An elegant way of achieving this is to emulate a multiscale molecular cloud with a power spectrum that follows a power law. We follow the procedure described in Koda et al. (2019). In addition, we insert two bright point sources, one in a bright and one in a faint region. We call the resulting model the “sky model.” The model has 4096^2 pixels with a size of $0''.05$ each, resulting in an image size of $204''.8$ on each side, shown in Figure 2.

With the sky model as input, we ran the `simobserve` task in CASA version 5.6.1 to create simulated observational data in MeasurementSet format. Following the ALMA Technical Handbook (Remijan et al. 2019), we adopted two configurations for the 12 m array (C-4 and C-1 in cycle 7), along with ACA 7 m and SD. The expected beam size for this configuration is $\sim 1''$ for an observing frequency of 115 GHz, and we covered 2 GHz bandwidth. The center coordinate of the field was set as (R.A., decl.) = ($12^{\text{h}}00^{\text{m}}00^{\text{s}}0$, $-35^{\text{h}}00^{\text{m}}0^{\text{s}}0$). For the 12 m (7 m) array, there are 52 (17) fields to cover the simulated image, and each field is set to be visited 30 (90) times per observing session on different days with an integration time of 10 s field^{-1} . The SD observation was set up with 169 fields, each visited nine times per day. Consequently, the total integration time to cover the sky model image with the 12 m/7 m/SD array is 1040/1020/3549 minutes. Both configurations of the ALMA 12 m array have the same integration time. This particular setup is to simulate a realistic ALMA observation and optimize (u , v) coverage. To ensure ideal (u , v) coverage even for the 7 m array at each field, observations for the 12 and 7 m arrays are set to be carried out over 4 separate days with a different hour angle at the start of observations, which is -2 , -1 , 0 , and 1 hr. For the SD array, observations are set to be carried out over 14 days due to the large number of fields. The achieved beam sizes are $57''$ for the SD data and $1''.2$ for the interferometric data. Relevant parameters for the simulated observations are summarized in Table 5.

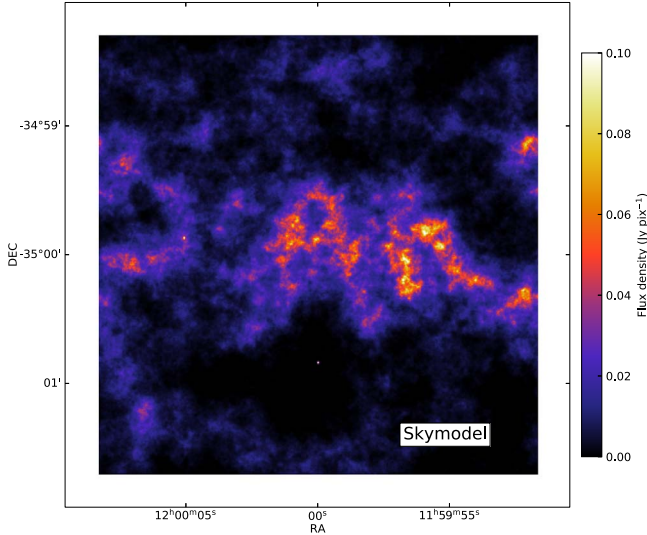


Figure 2. Synthetic sky model image used as input for the simulated observations.

Table 5
Details of the Data Sets

Parameter	Sky Model	M100
Phase center R.A.	12 ^h 00 ^m 00 ^s .0	12 ^h 22 ^m 54 ^s .900
Phase center decl.	−35 ^d 00 ^m 0 ^s .0	+15 ^d 49 ^m 15 ^s .000
Rest frequency	115 GHz	115.27120 GHz
V_{LSR}	...	1575 km s ^{−1}
ΔV (channel width)	...	5 km s ^{−1}
Velocity range imaged	...	[1400–1745] km s ^{−1}
Map size	204 ^{''} .8 × 204 ^{''} .8	400 ^{''} × 400 ^{''}
12 m array pointings	52	47
7 m array pointings	17	23
12 m array beam size	1 ^{''} .2 × 1 ^{''} .0 (PA = −84 [∘] .8)	4.0 ^{''} × 2.6 ^{''} (PA = −88 [∘] .2)
Range of 12 m baselines	[15–784] m	[15–200] m
Range of 7 m baselines	[9–45] m	[9–42] m

Figure 3 shows the images obtained from the simulated sky model observations with interferometry-only (hereafter *int-CLEAN*), the SD data only, and the different data combination methods (Feather, FSSC, SDINT, and MACF) described in Section 3 using both the simulated interferometric and SD data.

4.2. Observational, Spectrally Resolved Data

Working with real observational data, one can only make assumptions about the true sky brightness distribution. However, one condition that the combined interferometric and SD image must at least fulfill is that it recovers most of the flux visible in the SD image because in that image, no filtering of spatial frequencies has taken place.

Furthermore, as mentioned in the Introduction, there is a danger of deformation of the spectral features when no data combination is applied. So, the flux recovery condition needs to be tested for each spectral channel separately, and the results have to be compared between channels. Considering this, we therefore choose the spectrally resolved observation of the galaxy M100 as an example of real observational data.

The galaxy M100 (NGC 4321) was observed by ALMA as science verification²² data and has been featured in the CASA Guides series as an example of data combination using the Feather method.²³ The “grand design” barred spiral morphology of this galaxy, seen relatively face-on, reveals structures with different physical size scales. The data cube that we present here reveals the CO (1–0) (115.271 GHz, ALMA Band 3) molecular emission in 50 channels. On each side of the spectral line, 10 additional channels are included in the cube to show the spectral baseline. Observations were made of a 47-pointing ‘mosaic’ with the 12 m array, a 23-pointing ‘mosaic’ with the 7 m array, and an on-the-fly map with the SD array, effectively recovering a range of scales down to the 12 m array resolution of <2^{''}.

This data set allows us to showcase the necessary preparatory steps of header manipulation, axis reordering, and regridding. The observational details are given in Table 5. Figure 4 shows the interferometric and SD M100 images (in each case, the integrated emission over all 70 channels).

5. Assessment Metrics

Assessing the quality of the output image of a data combination is of utmost importance in the application and interpretation of the different methods (e.g., see Pety et al. 2013). The intrinsic definition of quality refers to the accuracy with which the combined data reproduce the true sky emission. In empirical research, the definition of an absolute quality assessment is hampered by the lack of a priori expectations for this true sky distribution. Instead, the quality assessment of a given target image $I_i(x, y)$ can be evaluated against the emission constraints present in a reference image $R_i(x, y)$. Here $I_i(x, y)$ is not necessarily identical to the data combination output image but can be a modified version of it, e.g., a version of this image convolved to the SD resolution.

This approach is motivated by our observational products. In real observations, the emission of any interferometric or data combination map can be compared against its SD counterpart in order to evaluate the total flux and emission structure recovered at the SD resolution. Following this same approach, synthetic interferometric data and combinations can also be evaluated against simulations at the maximum resolution provided by the interferometer once both are regridded into a

²² <https://almascience.org/alma-data/science-verification>

²³ https://casaguides.nrao.edu/index.php/M100_Band3

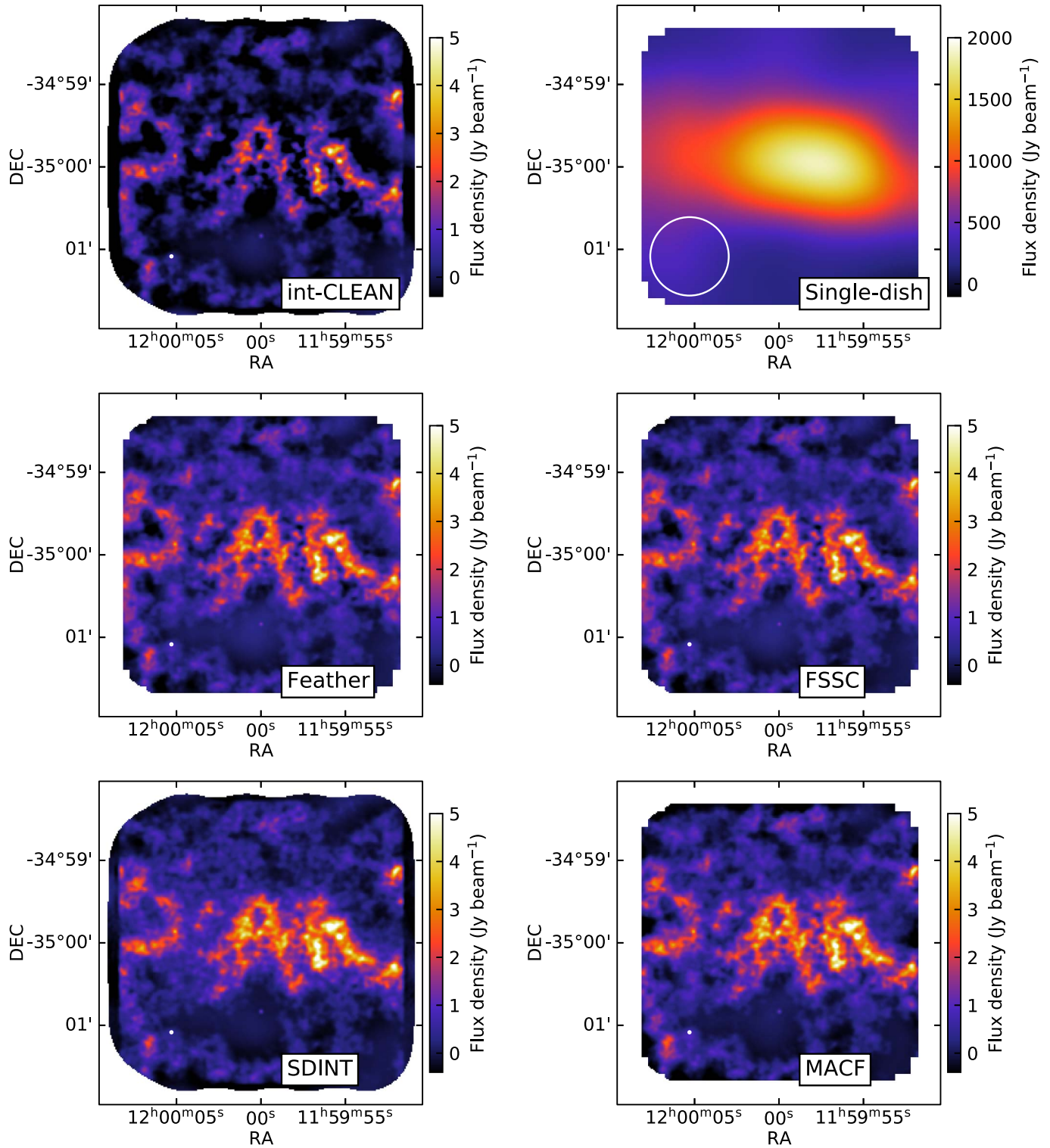


Figure 3. Maps of the simulated observations based on the sky model image in Figure 2 obtained with different combination methods. From left to right and top to bottom: int-CLEAN (interferometric-only), SD-only, Feather, FSSC, SDINT, and MACF. All interferometric and combined images are convolved into a final circular beam of $1''.7$ and displayed within the same color scale to facilitate their comparison. The beam size is indicated in the lower left corner of each image.

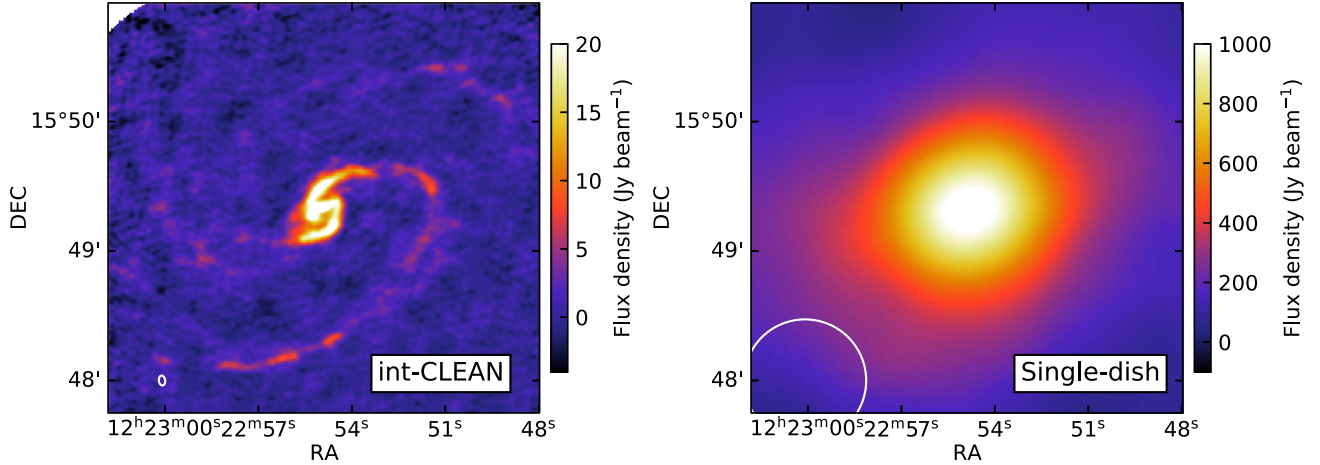


Figure 4. Integrated emission (moment zero, over all 70 channels) maps of our M100 data comparing the interferometry-only (left) and the SD image (right). The circles in the lower left corner represent the respective angular resolution (beam size).

common spatial and spectral coordinate system. Our analysis examines both the synthetic data from Section 4.1 and the real observations from Section 4.2.

We define as a reference image $R_\nu(x, y)$ either the SD image or the synthetic model used for comparison, while the target image $I_\nu(x, y)$ is assumed to be the combination result image convolved to the resolution of the reference image. For spectrally resolved data (cubes), our quality assessments will also detect variations of the quality with frequency, i.e., between channels.

We note that the effective comparison of the two images, $R_\nu(x, y)$ and $I_\nu(x, y)$, must be performed pixel by pixel at the same angular resolution (typically corresponding to one defined by $R_\nu(x, y)$, i.e., SD or synthetic model convolved to low resolution). Thus, if $I_\nu(x, y)|_0$ is the image at native interferometric resolution or the data-combined image, then $I_\nu(x, y)$ refers to the image convolved and (spatially and spectrally) regridded to the reference image parameters.

The spatial frequency filtering that occurs in interferometric observations usually affects the structure, spectral distribution, and absolute flux of the recovered emission. Assessing the quality of a given data set therefore requires considering fundamental parameters, such as the total recovered flux and its dependence on scale and intensity, as well as the variation of these indicators across the target field. These analyses should be carried out in statistical terms in both maps and cubes in order to make the assessment objective. In the following sections, we introduce a new set of image quality assessment metrics for the analysis of interferometric observations and their combination between multiple arrays and SD data, and we illustrate their use on the comparison of int-CLEAN and Feather method results. Feather is used as a benchmark of any combination technique presented here, since it is the most

common method used in CASA. Comparison of combination methods will be done in a later section.

5.1. Assessment Mask: Definition and Adaptive Thresholding

A detailed analysis of the image quality requires a careful definition of the so-called assessment region, that is, the subsample of (x, y) pixels (or (x, y, ν) voxels for cubes) in which our assessment metrics will be evaluated. Not necessarily all pixels in a map are relevant for the assessment of recovered flux. Regions devoid or showing low levels of emission should be used specifically for determining the rms noise of an image, as they are dominated by pure instrumental noise and otherwise excluded (masked out) from the image quality assessment. Ideally, any quality assessment should also consider the structure of the astronomical object, as well as include the instrumental response. The definition of assessment areas (e.g., rectangular region) or global intensity thresholds can simplify this analysis. To improve these basic—and sometimes arbitrarily defined—criteria, here we introduce a more general assessment mask, $AM_\nu(x, y)$, depending on the properties of the corresponding data products.

The definition of $AM_\nu(x, y)$ considers three conversion factors depending on the beam sizes θ_0 and θ_R of the (native) $I_\nu(x, y)|_0$ and $R_\nu(x, y)$ images, respectively, as well as the PB map $PB_\nu(x, y)$. The mask is determined according to the following steps.

1. We define the “mask threshold” at a level of $3 \times \text{rms}_{\text{mask}}$, where rms_{mask} is the off-source noise level of the target (in this case, interferometric) image at its native resolution θ_0 .
2. This single rms value is corrected for the effective antenna response in each pixel defined by the PB

correction per pixel, that is, $1/\text{PB}_\nu(x, y)$. The response per pixel is therefore $\text{rms}_{\text{mask}}/\text{PB}_\nu(x, y)$.

3. Next, the mask threshold needs to be evaluated at the reference resolution θ_R for our assessments and therefore corrected by a factor $\propto 1/\sqrt{N}$, where N is the number of θ_0 beams within θ_R , that is, $\sqrt{\theta_0^2/\theta_R^2} = \theta_0/\theta_R$.
4. Finally, the resulting mask threshold value, originally in units of flux per θ_0 beam, needs to be converted into θ_R units ($\propto 1/\theta_R^2$) requiring an additional θ_R^2/θ_0^2 factor.

Altogether, we thus define our assessment mask $\text{AM}_\nu(x, y)$ as

$$\text{AM}_\nu(x, y) = (3 \times \text{rms}_{\text{mask}}) \cdot \frac{1}{\text{PB}_\nu(x, y)} \cdot \frac{\theta_R}{\theta_0}, \quad (4)$$

where the ν subscript denotes that the mask can be applied to a single image or plane of a cube. We apply the same $\text{AM}_\nu(x, y)$ mask to both the $R_\nu(x, y)$ and $I_\nu(x, y)$ images, blanking all corresponding pixels where emission $R_\nu(x, y) < \text{AM}_\nu(x, y)$ at the reference resolution; in other words, the so-called ‘‘mask’’ retains the values where the assessment should apply. Compared to a single intensity threshold, $\text{AM}_\nu(x, y)$ effectively applies an adaptive thresholding, taking into account the different image resolutions and the spatial instrumental response, as well as channel-by-channel variations in emission structure (in the case of cubes), where the same mask is applied to all respective images.

5.2. Accuracy Parameter and Fidelity: Assessing Flux Recovery

The assessment of recovered flux has been quantified in several distinct but related ways in the literature since radio interferometers became available. A commonly used parameter is image ‘‘fidelity’’ (see, e.g., Cornwell et al. 1993, but a detailed definition follows below). This quantity is unsigned (i.e., does not indicate if too little or too much flux is recovered) and has no optimal value (its best value is ‘‘as large as possible’’). In this work, we introduce a new assessment parameter, which we call the ‘‘accuracy parameter’’ (A-par). The A-par is defined as

$$A_\nu(x, y) = \frac{I_\nu(x, y) - R_\nu(x, y)}{|R_\nu(x, y)|}, \quad -\infty < A_\nu(x, y) < \infty. \quad (5)$$

The A-par represents the relative difference between the flux of the input $I_\nu(x, y)$ and reference $R_\nu(x, y)$ images. The values of A-par range between negative and positive infinity. The ideal value is zero. The A-par is the signed relative error of the recovered emission after combination with respect to the reference image, where its sign indicates whether the emission is underestimated ($A_\nu < 0$) or overestimated ($A_\nu > 0$). A perfect match between the input $I_\nu(x, y)$ and reference $R_\nu(x, y)$ images thus corresponds to minimizing A-par in all pixels.

The A-par can be understood as the approximate inverse of the ‘‘fidelity’’ parameter (F_ν), such that $A_\nu(x, y) \approx F_\nu(x, y)^{-1}$. Note that fidelity is defined slightly differently by different authors. A compilation of the different conventions for ALMA, VLA, and ngVLA can be found in Mason (2021). We adopt the following definition:

$$F_\nu(x, y) = \left| \frac{R_\nu(x, y)}{I_\nu(x, y) - R_\nu(x, y)} \right|, \quad 0 < F_\nu(x, y) < \infty. \quad (6)$$

When used for image quality assessment, higher fidelity values indicate stronger similarities between the input $I_\nu(x, y)$ and reference $R_\nu(x, y)$ images (if $I_\nu(x, y) \sim R_\nu(x, y)$, then $F_\nu \gg 0$). Fidelity becomes a powerful assessment method for the relative flux comparison of distinct input images (e.g., $F_{\nu,1} > F_{\nu,2}$). However, as mentioned above, the target value of this fidelity parameter is, by construction, undefined (i.e., if $I_\nu(x, y) \rightarrow R_\nu(x, y)$, then $F_\nu \rightarrow \infty$), which limits its use during the assessment of individual images in absolute terms. In comparison, A-par provides additional information about the flux recovered (i.e., considering both A-par value and sign); therefore, we consider it more informative. Still, our analysis incorporates both A-par and fidelity assessments for a full description.

We calculate both A-par and fidelity parameters pixel by pixel (or voxel in cubes) in our images, that is, $A_\nu(x, y)$ and $F_\nu(x, y)$, for all pixels passing the assessment mask $\text{AM}_\nu(x, y)$ (see Section 5.1). We carry out these calculations by convolving and regridding both $I_\nu(x, y)$ and $R_\nu(x, y)$ images into a common beam θ and grid (x, y) , respectively, typically corresponding to those of the reference image $R_\nu(x, y)$. Additionally, we prefer to make assessments per pixel (Equations (5) and (6)) in order to portray the particular regions of the image that are more or less accurate, rather than effectively averaging over an entire image.

We show the A-par maps for the assessment of the data combination of our synthetic sky model data (Section 4.1) using int-CLEAN and Feather (Section 3.1) in Figures 5 and 6, respectively. In both figures, we display the reference (i.e., the true sky model; upper left panel) and target (interferometer-only or Feather image; upper right panel) images, both convolved into a circular beam of $2''$. An assessment mask as described by Equation (4) has been applied. The masked out pixels are shown with white in the upper two panels of the figure. The lower panels show the A-par map (lower left panel) and histogram obtained from the pixel values of the A-par map (lower right panel). Figure 7 shows similar plots but for the fidelity parameter. This representation allows us to intuitively identify variations of flux recovered in different regions of our maps (A-par or fidelity maps), as well as to statistically describe these properties over the target field (histograms).

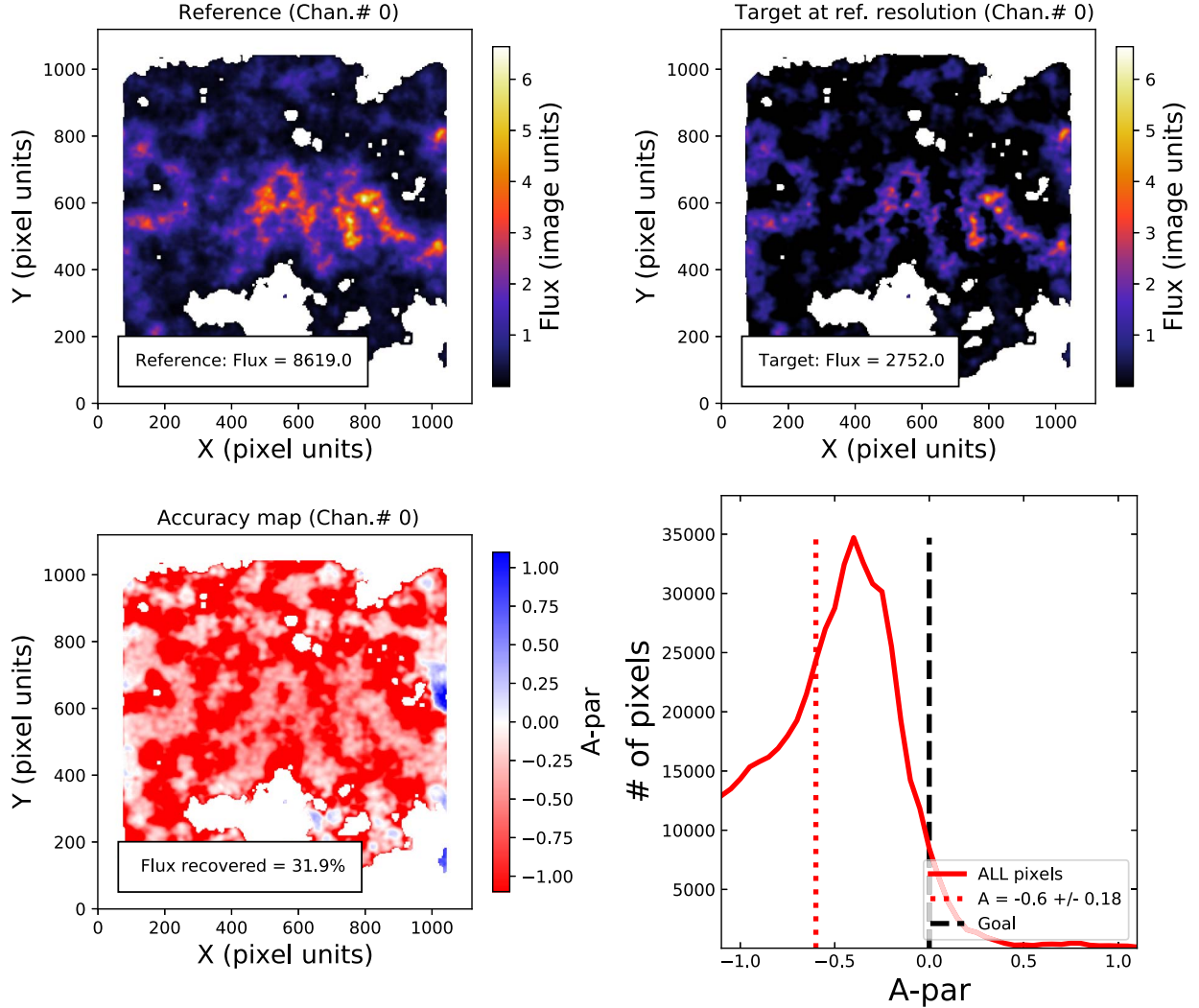


Figure 5. The A-par assessment for the int-CLEAN reduction of our synthetic continuum sky model data (Section 4.1): (upper left panel) sky model used as reference image $R_r(x, y)$, (upper right panel) Feather image used as target $I_t(x, y)$, (lower left panel) A-par map, and (lower right panel) A-par histogram. Note that all results are obtained at a common resolution of $2''0$ and display all pixels within the assessment mask $AM_i(x, y)$ (in color). Total flux values for the sky model (reference; top right) and int-CLEAN (target; top left) images, as well as the amount of flux recovered (bottom left), are indicated in the legends. The histogram also includes the mean and standard deviation values for the observed A-par distribution. The vertical dashed lines show the mean A-par (red) and its desired value zero (black).

The analysis of the histograms and distribution of the A-par values in our images allows us to quantify the quality of an imaging technique (see Figures 5 and 6, lower right panel). The mean value and dispersion of such distributions provide information about the typical fraction of recovered flux per pixel. High-quality data combination techniques would produce A-par histograms with mean values close to zero ($A = 0$) and a small width ($\sigma(A) \rightarrow 0$) showing a narrow width distribution that is approximately Gaussian.

Similar comparisons using fidelity would produce distributions with increasingly high peaks and more pronounced skewness toward large fidelity values. In both cases, the

inspection of the A-par and fidelity maps (in Figures 5–7) can be used to identify spatial variations and systematic effects on the quality of the data.

Multiple histograms can be overplotted in order to compare different images obtained from the same observation. We show an example of such a comparison in Figure 8 (left panel), which illustrates the very significant improvement on the recovery of the true sky emission produced by applying a data combination technique (here Feather, orange histogram; $A\text{-par} \approx -0.08 \pm 0.24$) in comparison to using the interferometric-only int-CLEAN reduction (red histogram; $A\text{-par} \approx -0.60 \pm 0.43$). These improvements translate into the total amount of flux recovered in

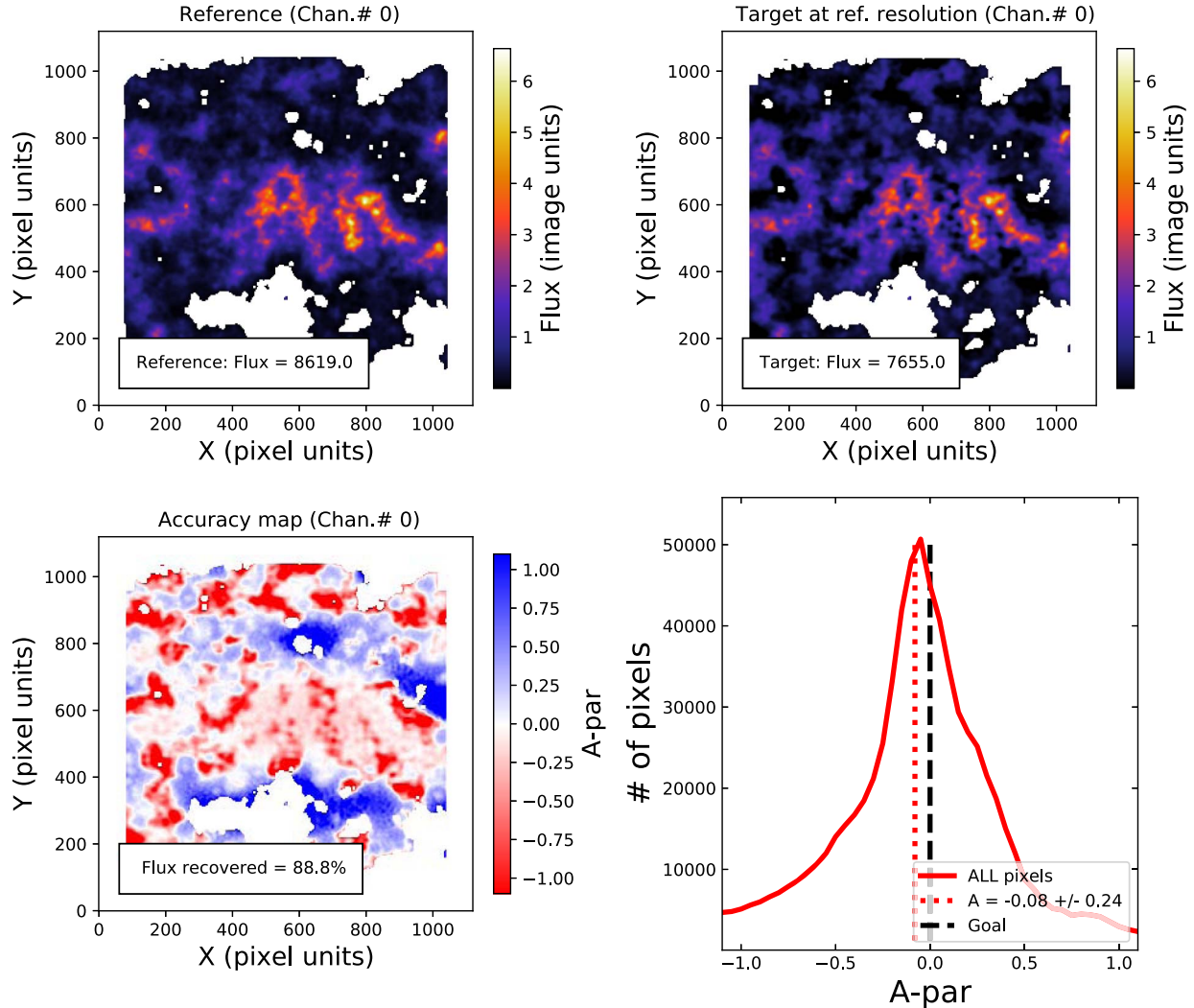


Figure 6. The A-par assessment for the Feather of our synthetic sky model data (see also Figure 5).

each case. While int-CLEAN only recovers $\sim 32\%$ of the total reference flux, Feather manages to improve these values up to 89%.

5.3. A-par versus Flux: Flux Recovery as a Function of Intensity

The distributions of the A-par and fidelity parameters provide information about the global properties of the flux recovery in our data. However, the fraction of recovered flux in the target image depends on the sky brightness temperature. This is particularly true if the target field exhibits large regions with low-intensity but extended flux in comparison to bright and compact emission spots (see variations of the corresponding A-par and fidelity maps in the lower left panels of Figures 6 and 7, respectively). In these cases, it is instructive to investigate not only the total A-par distribution (Section 5.2)

but also the variation of this parameter as a function of the reference flux.

We investigate the dependence of the flux recovery as a function of flux in Figure 8 (right panels). We represent the fraction (percentage) of the flux recovered in individual (top panel) and cumulative (bottom panel) diagrams. Critical for their interpretation, we overplot the contribution of the reference flux (again per flux bin and cumulative, respectively) in both panels. Maximizing the flux recovered is key for any data combination method and most significant in the case of flux bins with large contributions to the total image flux. In our sky model example, bins with intensities between ~ 0.4 and 4.0 (in image units) each contribute $>10\%$ of the total flux of the reference image (see gray distribution in top right panel, with reference to the right y-axis also in gray) becoming the most relevant flux bins.

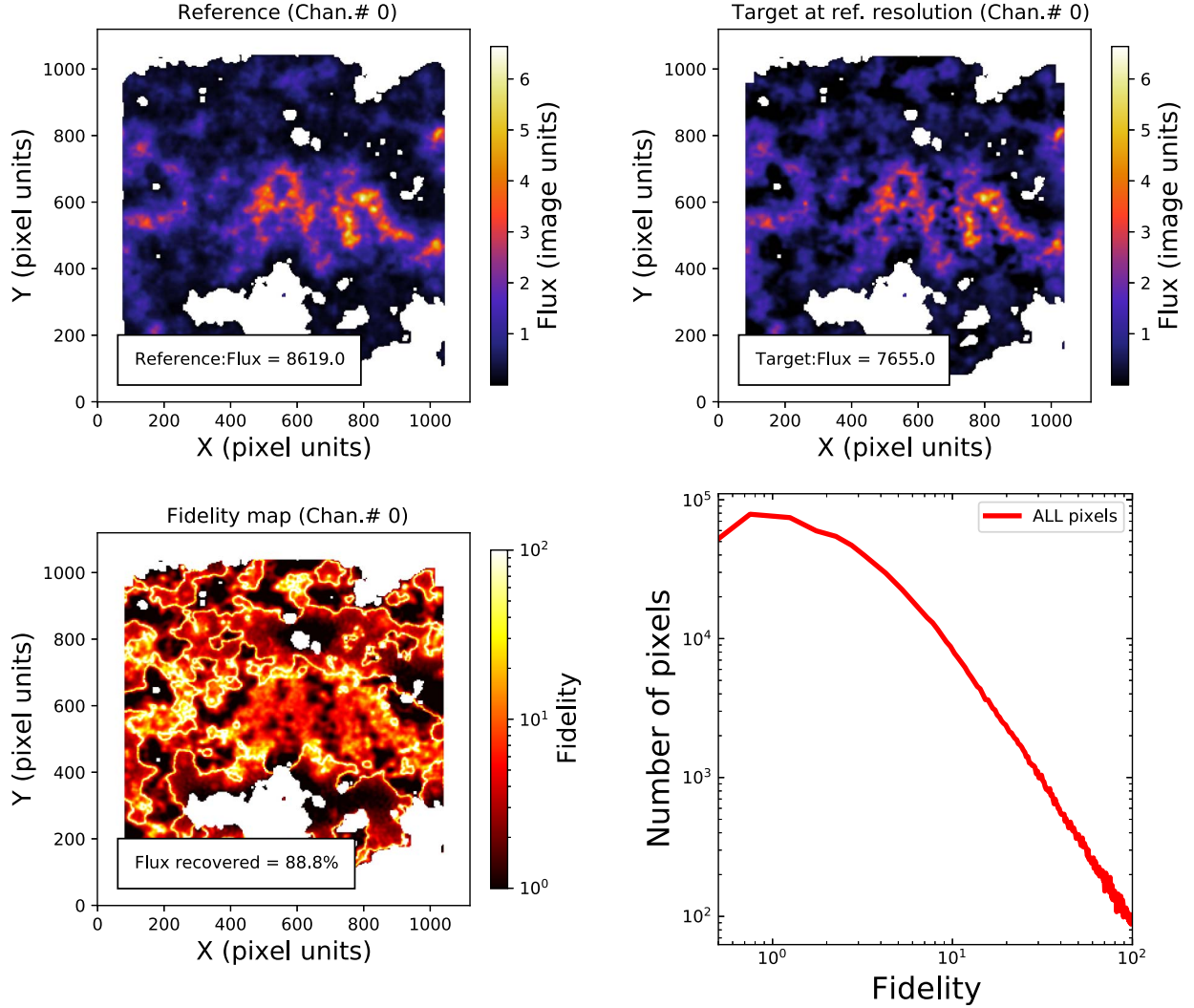


Figure 7. Fidelity assessment of using Feather on our sky model data (Section 4.1). Panels are analogous to those for A-par in Figure 6, except that here a mean value is not plotted, since the shape of the distribution is not well characterized by it. An ideal value does not exist by definition.

In the lower panels of Figure 9, we show a direct pixel-by-pixel comparison between the reference flux $R_\nu(x, y)$ in the sky model and the recovered flux $I_\nu(x, y)$ by our Feather combination within $AM_\nu(x, y)$. Similarly, we show the variation of the A-par values as a function of $R_\nu(x, y)$ in the upper panels, including the mean and sigma values (dark blue) and interquartile [Q10, Q90] limits (cyan) in 10 flux bins. In this representation, a perfect data combination should produce a linear correlation between the $R_\nu(x, y)$ and $I_\nu(x, y)$ fluxes (i.e., a straight line in the lower panels) with a narrow distribution independent of the reference flux (i.e., A-par consistent with noise) in the upper panels.

The analysis of these diagrams permits a direct evaluation of the dependence of the flux recovery with intensity in real data

combination techniques such as the one shown in Figure 9. Our quality assessments demonstrate how pure interferometric data fail to recover the expected reference flux distribution at all intensities (A-par < 0 in all flux bins; see Figure 9, left panels). These issues also affect the regions with the highest intensity and compact emission with average flux losses of about 25%. More importantly, the performance of pure interferometric data processed with CLEAN shows a strong dependence of A-par on flux, producing worse results at lower signal values. In comparison, Feather shows a clear overall improvement on the flux distribution recovery at all intensities with A-par values of $\approx 0 \pm 0.5$ in all of our signal bins, as expected from the analysis of the total flux recovery ($A = -0.07$ or -7% mean offset; see Figure 8). Despite these improvements, our analysis reveals an

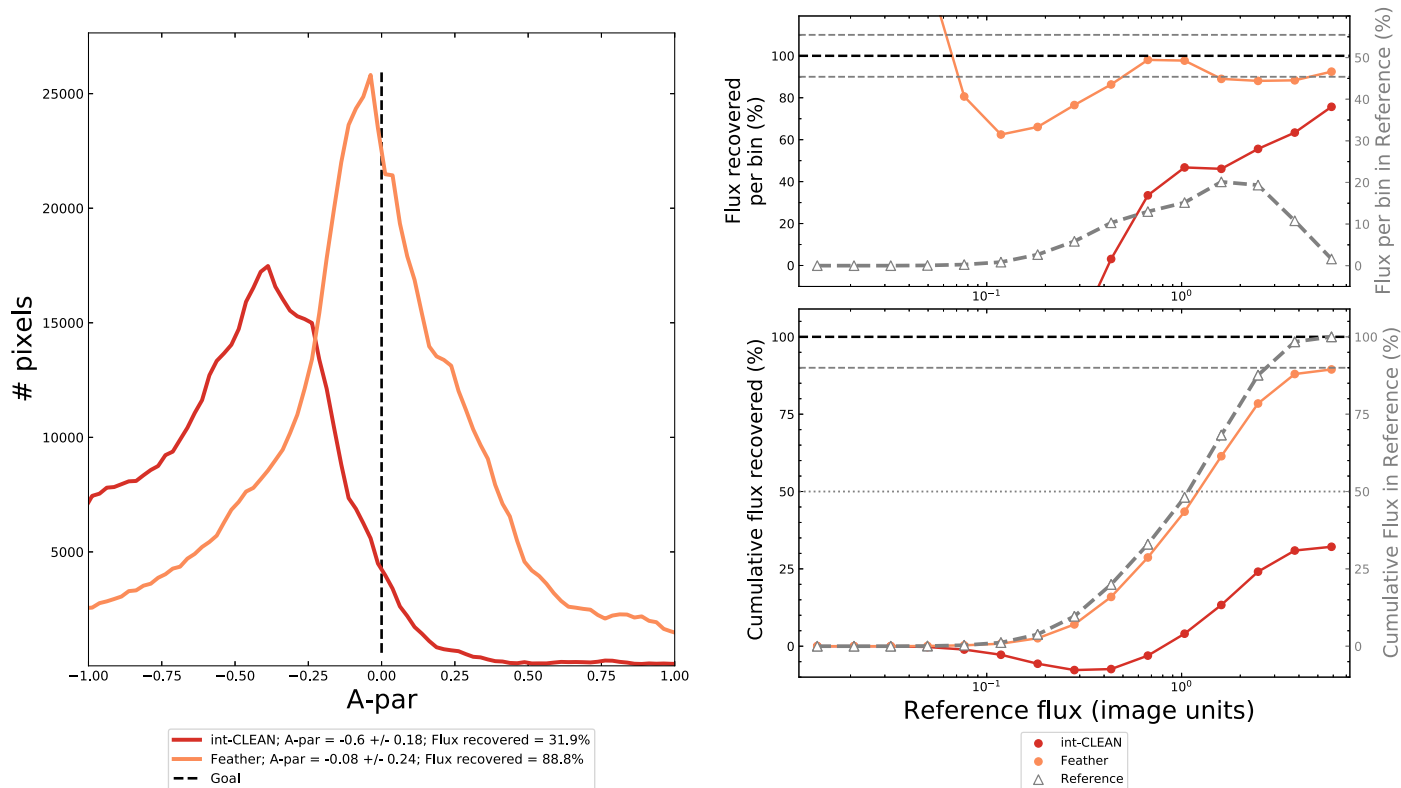


Figure 8. Comparison of the A-par distributions for the interferometer-only CLEAN (red) and Feather-combined (orange) results on our sky model data. (Left panel) Histogram of all A-par values within our assessment area, where a perfectly recovered pixel would contribute a value of zero. (Right panels) Flux recovered per flux bin shown in individual bins (top) and cumulative (bottom). In both plots, the corresponding flux of the reference image, i.e., the expected recoverable flux, is shown in gray and corresponds to the right axis, also in gray. In the top right panel, the flux recovered per bin is shown in percentage with respect to the total flux in the image (see right vertical axis). Horizontal dashed lines with guiding values of $100\% \pm 10\%$ in the top right panel and 50%, 90%, and 100% in the bottom right panel are included to improve the readability of the plot.

increase of the dispersion of A-par values at lower signal values, indicating that, although better than a pure CLEANed interferometric data, the performance of Feather may be hampered in regions of low-intensity emission (see a more detailed discussion in Section 6).

The enhanced image quality indicated by A-par both globally (Figure 8) and per signal bin (Figure 9) corresponds to an improved flux recovery by a combination technique, in this case, Feather (e.g., see Figure 6), compared to interferometric-only maps. An ideal data combination should, in principle, maximize the flux recovery at all scales. In practice, however, this may not be possible or critical since, depending on the emission distribution, not all signal bins may contribute equally to the total flux budget. This is illustrated in Figure 8 (right panels), where we show the percentage of flux recovered per signal bin independently (top panel) and cumulatively (bottom panel) with respect to the reference image. The dashed gray line in the top panel indicates the contribution of each individual signal bin to the total flux budget. We point out that for the sky model data, bins with intensities of >0.2 (in image

units) contribute most of the emission within the assessment area ($>80\%$ of the total). Recovering the flux in those bins therefore guarantees the recovery of a significant fraction of the total image sky brightness temperature. The analysis of these plots also highlights the poor performance of int-CLEAN, producing negative flux values (due to PSF side lobes plus filtering effects) in regions with extended emission showing emission values of <1 (in image units) and leading to flux recovery values of only 25% of the total flux.

The high sensitivity of the above comparisons demonstrates the robustness of our assessment metrics. Additional tests indicate that deviations at different flux intensities may also reveal potential issues in the data combination process (e.g., recovery of extended emission) and/or the limitations of such procedures (e.g., lack of baseline overlap). Moreover, this analysis permits one to investigate the performance of different data combination techniques and their response to images with different dynamic ranges in emission (see discussion of the data combination results in Section 6).

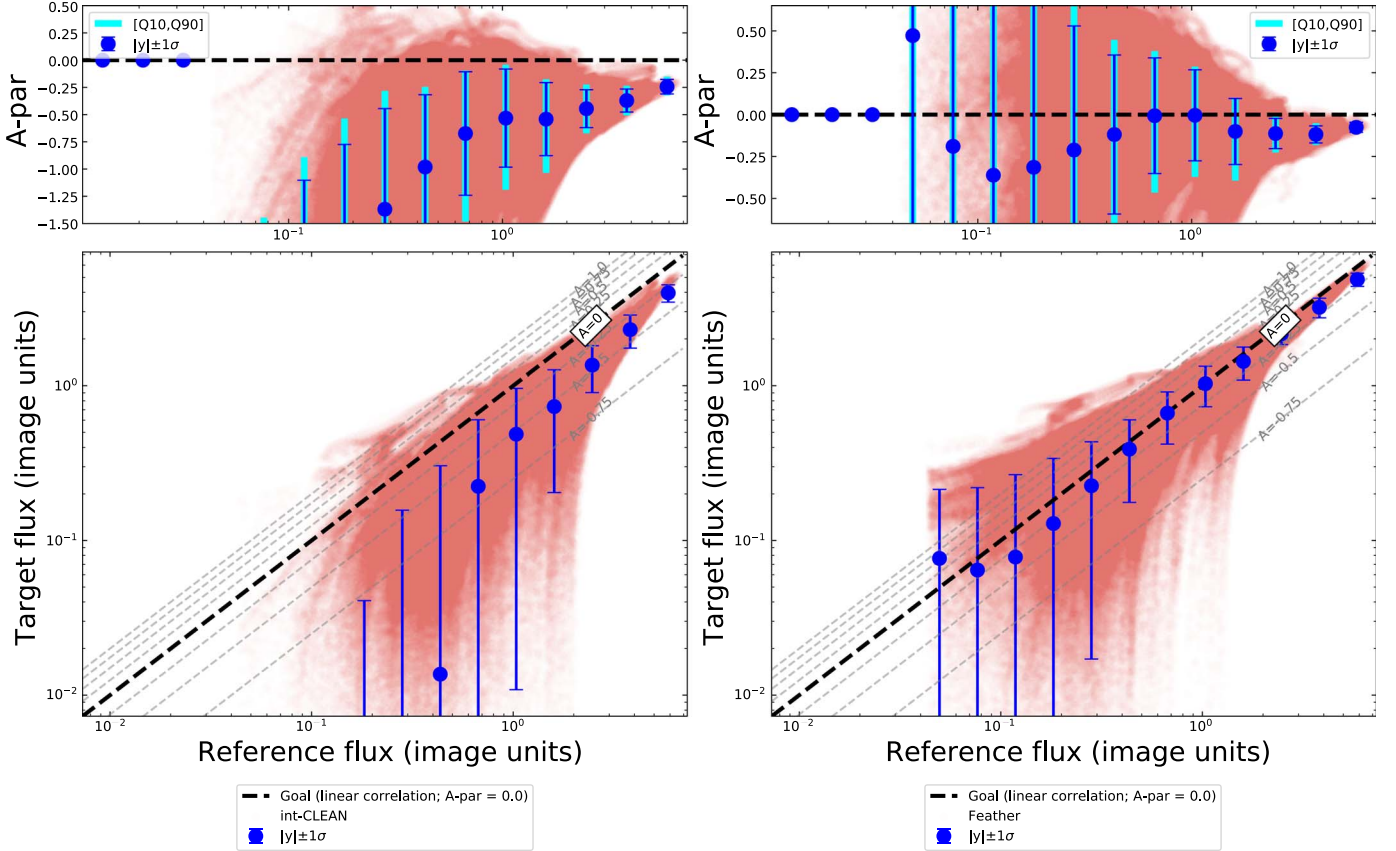


Figure 9. The A-par values as function of intensity for both int-CLEAN, i.e., pure interferometric data (left), and Feather (right) methods for our sky model synthetic data. Lower panels: pixel-by-pixel comparison between the reference flux $R_i(x, y)$ and recovered flux in the target image $I_i(x, y)$ for pixels included in the assessment mask $AM_i(x, y)$ (red points). The dashed lines indicate the expected correlations for different A-par values. Upper panels: individual A-par $A_i(x, y)$ values as a function of the reference flux $R_i(x, y)$. We represent the mean and standard deviation in 10 intensity bins in dark blue. Also, we display the interquartile [Q10, Q90] range in cyan. In both the lower and upper panels, we indicate the expected distribution limits for the case of perfectly recovered emission (i.e., $A = 0$) showing only white-noise deviations with $\sigma = 0.1$ (in image units).

5.4. Power Spectra: Spatial Scale Sensitivity

The primary goal of each data combination method is the successful recovery of emission at the angular scales filtered out by the interferometer. Thus, it is crucial to describe how the recovered emission is distributed as a function of angular scale. One such tool is the spatial power spectrum (SPS), defined as

$$P(k) = \mathcal{F}[I_\nu(x, y)] \mathcal{F}^*[I_\nu(x, y)], \quad (7)$$

where k is the wavenumber ($k = \frac{1}{\theta}$, where θ is the angle on the sky in radians), and \mathcal{F} is the FT of the input image, $I_\nu(x, y)$, under study. This is a two-point correlation function that measures how power (i.e., structure) is distributed across spatial scales. In practice, the distribution of power is measured by computing the 2D FTs of the integrated intensity images and measuring the median in progressively larger annuli. We chose the median to mitigate the bias introduced by ringing artifacts of the *sinc* function along the axis of the 2D FT when emission extends toward the edge of the image. While phase

information is lost due to multiplication by the complex conjugate, comparing the SPS profiles derived from the images produced by the various combination methods to the input reference (or TP) demonstrates how successfully the emission is recovered across the full range of angular scales. The ideal image would recover the flux of the input model image on all scales.

As an example, we present in Figure 10 the SPS profiles measured for the data combination of our sky model using Feather in comparison to the interferometer-only data processed with CLEAN. Also shown is the profile of the original input image of the simulation (“reference”). These three profiles agree remarkably well at larger angular scales (left side of the plot). Feather and reference continue to agree all the way down to the smaller angular scales accessible to the instrument. But the int-CLEANed interferometer-only data start to diverge from the reference as the scale size decreases. This result can be understood by considering the way the power is

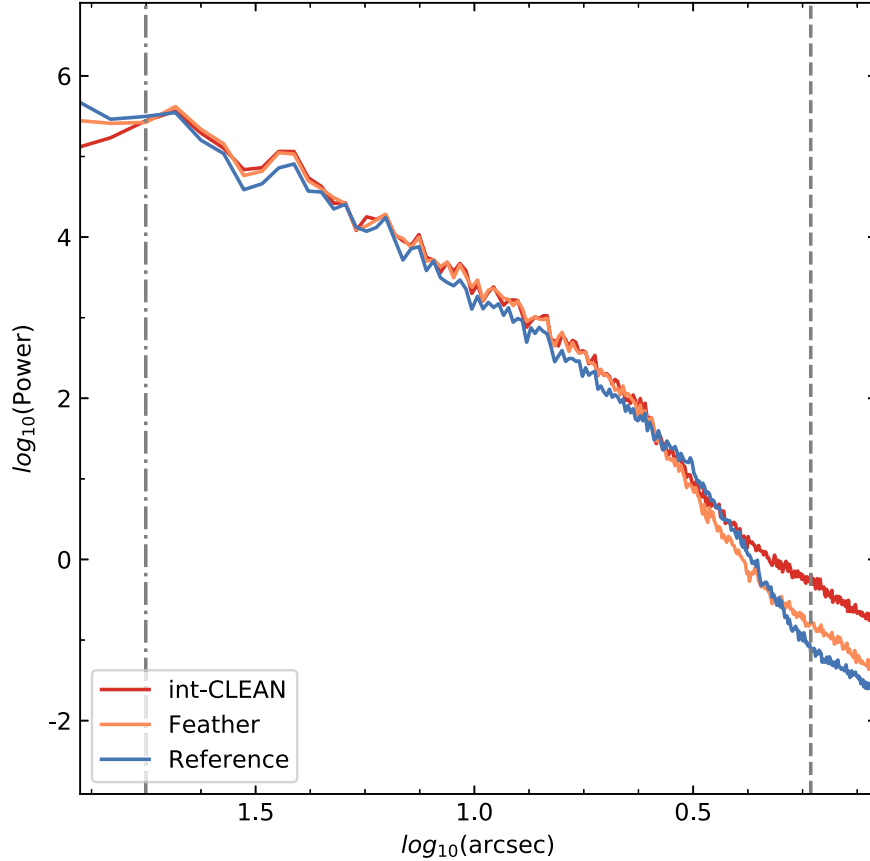


Figure 10. The SPS obtained from the pure interferometric data (int-CLEAN; red) and Feather-combined interferometric and SD data (orange) compared with the original power spectrum of our sky model simulation (blue). Note the logarithmic scales and the several orders of magnitude of flux present in the input model image. Vertical lines show the final image resolution (dashed line) and largest angular scale effectively sampled by the SPS (one-third of the map size; dotted-dashed line), beyond which this simulated instrument is not sensitive.

measured; the insufficient recovery of the larger scales effectively boosts the intensity contrast of the already existing small-scale structure in the interferometer-only image leading to higher power (i.e., larger differences) at small angular scales compared to the reference image. Conversely (not shown in this example), when the SD data are given too much weight in the combination, the power decreases at small scales because the low-resolution SD data effectively wash out the observed small-scale structure. The variation in power at small scales highlights subtle deficiencies that may not be immediately and clearly visible in the images. Scales below the beam size (right of the dashed line in the figure) are dominated by correlated noise in the pixels or convolution residuals and should generally be ignored.

The above SPS analysis can also be applied to the case of our A-par maps (e.g., Figure 6, lower left panel). The expected A-par power spectrum provides information on the variance of the relative errors, $\sigma(\text{A-par})$, as a function of scales (e.g., high A-par power denotes large systematic errors at a given scale). In addition to the minimization of the (global) A-par mean and

dispersion values (e.g., in Figure 8), the goal of any data combination method is therefore to minimize the A-par SPS, that is, all systematic errors as a function of scale. We show the results of the A-par SPS for our int-CLEAN and Feather reductions in Figure 11. Our results illustrate the reduction of the A-par variance at all scales once a Feather combination is applied to the original int-CLEAN reduction. The interpretation of these results in comparison with other combination methods and the addition of Gaussian noise to our reference sky model is discussed in Section 6.4.

5.5. Using SD Observations as Reference Image

Unlike the case of our synthetic sky model as presented in our previous assessments, the quality assessment of real scientific data sets is usually hampered by the lack of information for reference at high spatial resolution. Instead, when considering total emission on all scales, interferometric observations can only be cross-checked with the flux measurements obtained at SD resolution. Such comparison requires the

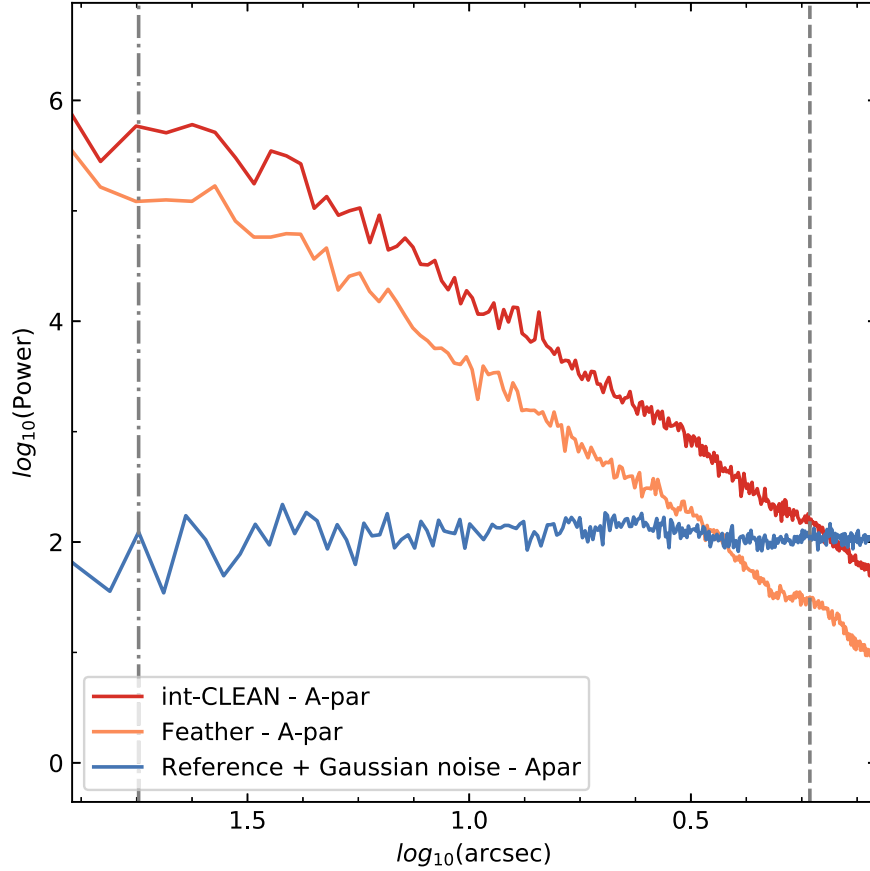


Figure 11. The A-par SPS for the same int-CLEAN and Feather data reductions shown in Figure 10. For comparison, we add the expected (flat) A-par power spectrum of our reference image with Gaussian noise added.

original interferometric image at its native (high-)resolution $I_v(x, y)|_0$ to be convolved into a final (low-)resolution image $I_v(x, y)$ similar to the SD data $R_v(x, y)$.

We quantify the effects of this low-resolution comparison in our assessment metrics in Figure 12, showing the results of int-CLEAN (red) and Feather (orange) for our sky model simulation, this time convolved into the SD resolution ($57''$), for the case of the A-par statistics (left panel) and the recovered flux per signal bin (right panel). Figure 12 can be directly compared with Figure 8, carried out at much higher resolution ($1''.7$). Several results can be taken from this comparison. The number of pixels for the quality assessment is largely reduced due to the use of a much larger beam size, as seen in the overall pixel statistics. Changes in the beam size also alter the local A-par estimates due to the averaging of regions with/without emission within the much smoother SD beam. Nonetheless, our assessment metric preserves the relative differences between methods. Both the A-par statistics (left panel) and the recovered flux (right panel) indicate the improved performance of data combination techniques such as Feather in comparison with interferometric-only CLEAN deconvolution.

Several caveats should be considered during the quality assessment of images at the SD resolution. First, and by construction, the SD observations only provide information on the total flux per SD beam, but the emission distribution at smaller scales remains unconstrained. Second, large convolutions (such as the one shown in Figure 12) can lead to averaging effects of multiple emission features at interferometric resolutions (e.g., compact sources and negative side lobes) unresolved at the SD beam size. Third, the limited number of resolution elements in the SD images restricts the use of some size-dependent assessments, such as SPS. Treated with caution at low resolutions, however, our assessment metrics provide a powerful toolkit to assess the quality of both continuum and spectral interferometric observations.

5.6. A-par Spectrograms: Analysis of Spectral Cubes

In order to extend the previous assessments, which were of a continuum (single-channel) image, to a data cube, we must visualize the variation in the spatial distribution as a function of frequency (or velocity) channel. This is important because the astronomical objects are likely to have distinct

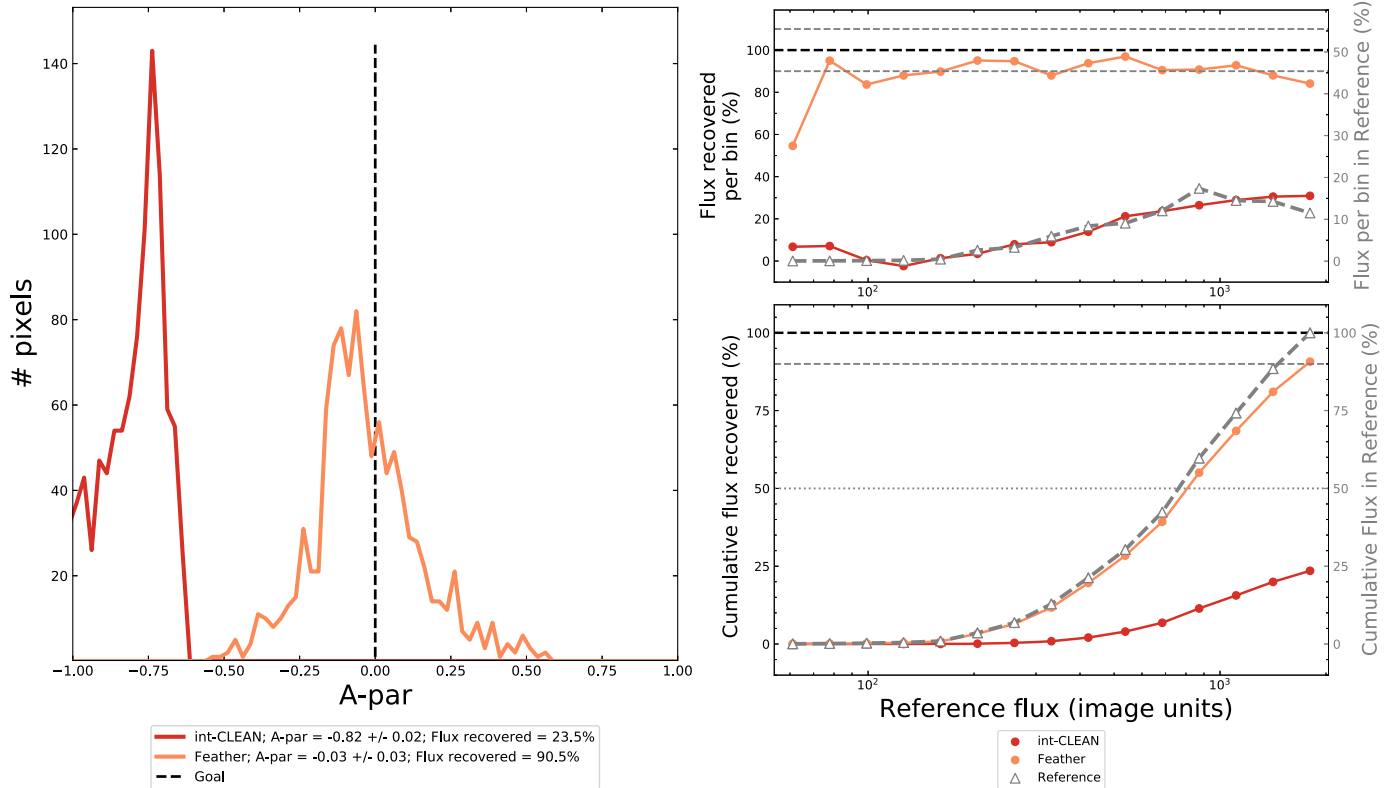


Figure 12. Same as Figure 8 but using the SD image as reference rather than the simulation input image, as would be done when working with real observational data.

morphologies for material at different velocities. Hence, any combination method, or perhaps no combination, might be sufficient for the channels with more compact emission, whereas the channels with more extended emission depend much more on the combination for an acceptable image quality.

We extend the A-par analysis from the previous continuum case (e.g., Figure 10) to that of a cube in the form of an A-par spectrogram, shown in Figure 13. This spectrogram shows the distribution of A-par values for all channels in the target cube that satisfy our assessment mask $AM_r(x, y)$ criteria (left panel). For a given velocity channel (x -axis), the spectrogram shows the number of voxels within this frequency plane (color scale) with a given A-par value (y -axis). Its analysis provides a visual comparison of the emission recovered in multiple channels and allows the evaluation of local (per channel) and global (mean distribution) deviations, as well as issues (e.g., outliers and/or problematic channels) in the data. Similar to the analysis of the continuum images, the goal of any data combination method is to minimize the absolute value of this A-par spectrogram for all channels within a cube. We complement these results with additional histograms (right panel) for A-par showing all

individual channel values (gray histograms), as well as the mean distribution (red histogram).

These spectrograms turn out to be a powerful and intuitive tool when comparing multiple data combination techniques in large spectral cubes. In Figure 13 (top panels), we again illustrate the limitation of the interferometer-only emission recovery ($A\text{-par} < 0$) at different velocities/channels. Moreover, our spectrograms illustrate how the flux losses also depend on velocity, since the brightness distribution also varies with velocity (see Section 6.2). Depending on the selected channel, A-par varies between ~ -0.1 (10% flux losses) and > -0.5 ($> 50\%$ flux losses). In contrast, data combination with Feather (bottom panels) produces significantly better results at all velocities/channels with typical values of $|A\text{-par}| \sim 0.2$ (or $\pm 20\%$ error) for most channels (between [10, 60]). The improvement is also seen in the mean A-par values in the corresponding histograms. The broad and shifted distribution in the int-CLEAN reduction with mean 50% flux losses ($A\text{-par} = -0.51 \pm 0.07$) is significantly improved by Feather showing a narrower and more centered distribution showing differences of less than 10% with respect to the SD flux per channel ($A\text{-par} = -0.07 \pm 0.04$).

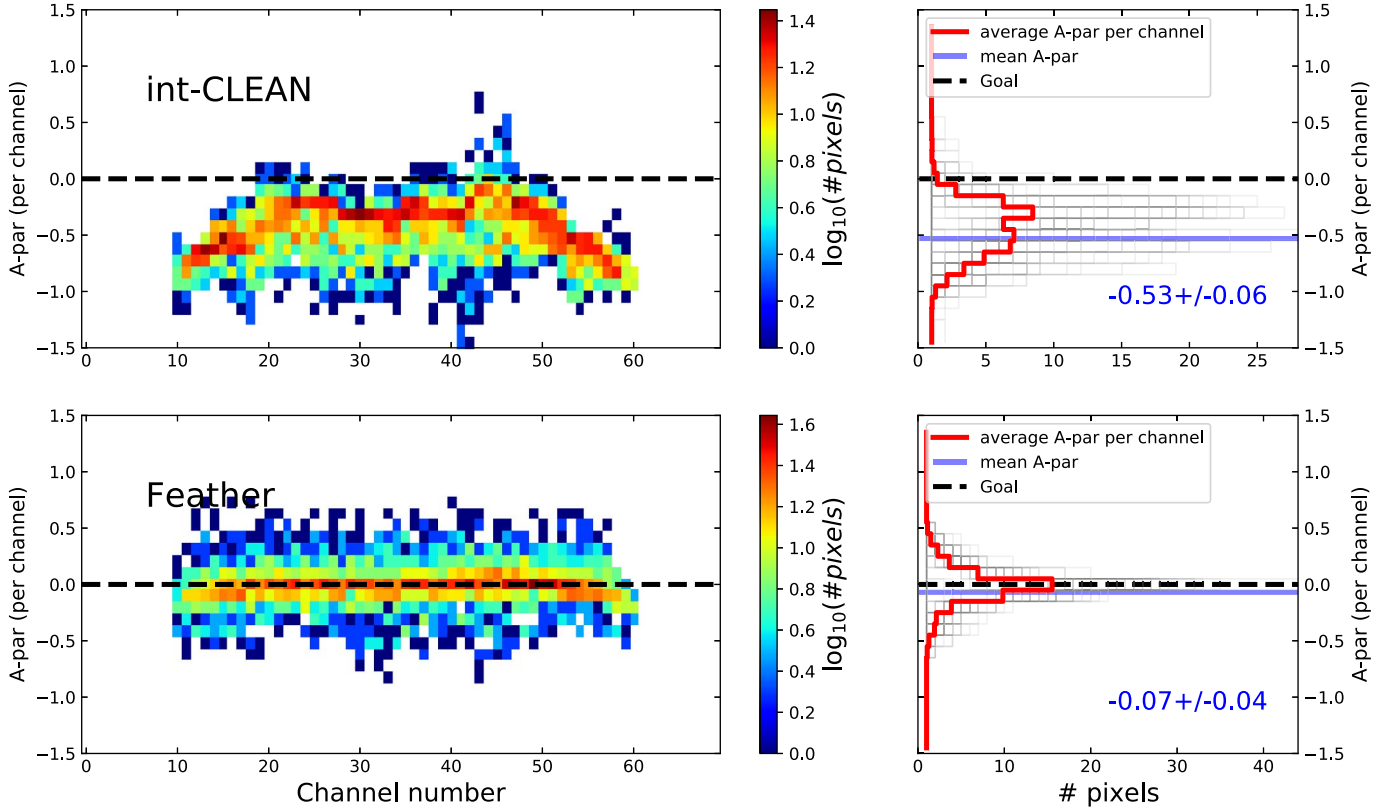


Figure 13. The A-par spectrogram for our M100 data obtained from the interferometric data alone with int-CLEAN (top) and from the Feather-combined interferometric data and SD image cube (bottom) for all voxels within our assessment mask. The detected emission in each spectral channel of this CO line observation represents emission from gas at a specific velocity range with its own spatial distribution.

A variation of A-par with channel directly translates into a deformation of spectral line features, as will be discussed in Section 6.2. That is the case for our int-CLEAN reduction, as seen in Figure 13 (top panels). In other words, data combination is also relevant for spectroscopy.

6. Combination Method Comparison and Discussion

6.1. The Indispensable Short-spacing Information

The results presented in Section 5 demonstrate the large impact of the short-spacing information on the analysis of interferometric observations. All assessment metrics show significant improvements of the flux recovered at different spatial scales and input signals using a standard data combination technique such as Feather when compared to pure interferometric-only CLEAN (int-CLEAN) reductions (see Figures 6–13). Here we explore the relative performance of alternative data combination techniques.

We highlight the enhanced image quality of different data combination techniques in Figure 14 by comparing our input sky model emission (reference; top left panel) with the results obtained by int-CLEAN (top right panel), Feather (bottom left

panel), and SDINT (bottom right panel) in the central region of the sky model image (see also Figure 3; FSSC and MACF maps are not shown, as they produce visually similar results to Feather and SDINT, respectively). This region is selected because it incorporates both compact and extended emission. A direct inspection of these images reveals how pure int-CLEAN deconvolutions (top right panel) miss large fractions of the true sky emission at all scales and flux values due to the incomplete sampling of the (u, v) space in interferometric-only observations when extended sky emission is present. The resulting interferometric filtering becomes nonintuitive, showing highly nonlinear effects in the case of complex sources and leading to a flux recovery of only $\sim 10\%$ – 20% of the true sky emission (see Figure 8, red lines). These effects can sometimes be identified in our images by the appearance of regions with negative emission (negative side lobes; dark areas in the int-CLEAN image).²⁴

²⁴ We note here that the absence of negative emission troughs in the image does not guarantee the absence of filtering, as the effects of filtering can be compensated for by the presence of additional positive emission, depending on the source structure.

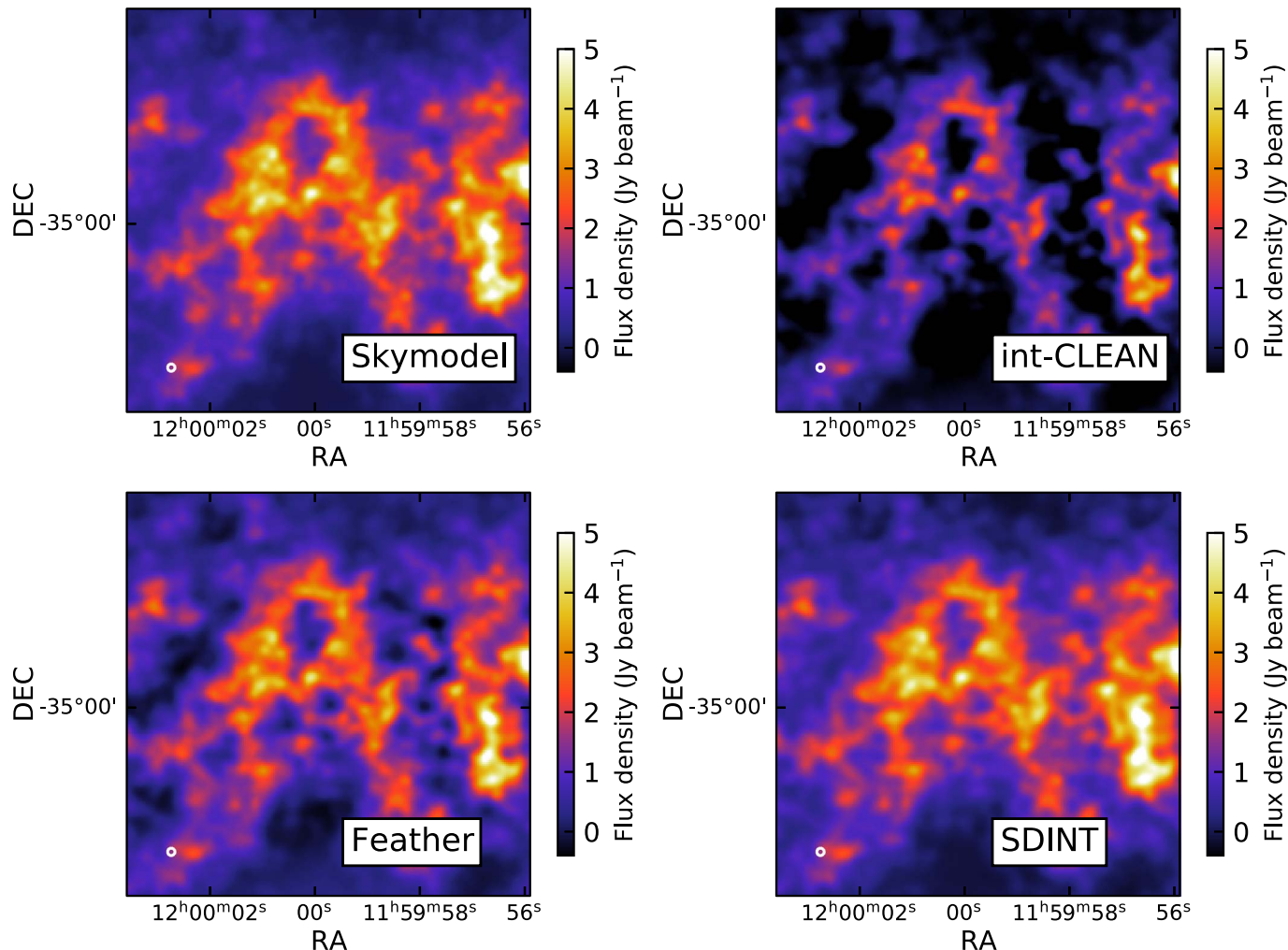


Figure 14. Comparison of the true sky brightness distribution with the recovered emission of interferometry-only and two different data combination methods in the central region of our sky model: (top left) sky model image (i.e., reference), (top right) int-CLEAN (i.e., only interferometric data), (bottom left) Feather, and (bottom right) SDINT, all convolved to a common resolution of $1''.7$ (see beam size in the lower left corner) and shown with the same intensity scale.

Interferometric-only observations (int-CLEAN) are expected to efficiently recover the total flux of unresolved, isolated sources with sizes comparable to the interferometer beam size. However, this situation is not the same in the presence of smooth, extended emission. In the latter cases, it is sometimes assumed that the lack of short-spacing information only affects the recovered emission beyond the maximum recoverable scale (MRS)²⁵ sampled by the interferometer. But our results clearly demonstrate how the interferometric filtering has a significant impact at all scales, including those compact regions with sizes comparable to the beam size (i.e., angular scale \ll MRS).

²⁵ See Remijan et al. (2019) for a definition. The MRS depends on the details of the interferometric array setup. For the ALMA 12 m nominal configurations with 43 antennas, the MRS is approximately a factor of 10 larger than the achieved angular resolution.

The addition of the short-spacing (SD) information dramatically improves the image quality. Standard techniques such as Feather (Figure 14, lower left panel) recover up to $\sim 90\%$ of the input sky model emission (see Figure 8, blue lines) and remove most of the negative emission patches in the field of interest.

The addition of the short-spacing information at low resolutions also has a direct impact on the peak flux in many of the compact sources in this region, potentially affecting column density and mass estimates in subsequent scientific analysis. We demonstrate these issues in Figure 15 by comparing the emission recovered by int-CLEAN, Feather, SDINT, and MACF at the central region of our sky model showing multiple compact emission features with sizes comparable to the beam size. For illustrative purposes, we compare the emission profile of the brightest region within this field (see bottom right panel). Although compact, the peak flux

of this source in the interferometric-only int-CLEAN observations is reduced by a factor of $\sim 40\%$ compared to the true emission in our sky model. Flux losses are also seen in other nearby sources, together with negative side lobes in regions with fainter emission (see also top right panel). Still, the effects on our maps depend on the location of the source and the structure of its surroundings, making a direct correction without the zero-spacing information impossible. The use of data combination techniques significantly improves the flux recovery in these compact regions with, in our particular case, SDINT and MACF producing the best results. These reported differences could have a significant impact on derived properties such as mass and column densities of compact sources in complex environments. These results underline the absolute need for short-spacing information and data combination in the analysis of particular high dynamic range observations provided by state-of-the-art interferometers such as ALMA.

6.2. Effects of the Short-spacing Information in Line Profiles

So far, the discussion has focused on the analysis of the integrated emission maps. As introduced in Section 5.6, the extent of the effects of a lack of short-spacing information will depend on the target structure in each frequency channel. We illustrate these effects in Figure 16 in two representative regions in our M100 data set. As shown in Figure 16 (left panel), the interferometric filtering produces changes of up to 50% of the flux per channel in this spectrum. The true spatial structure of the emission and thus the fraction of missing observed flux is, however, not necessarily homogeneous but can vary from channel to channel. According to Figure 13 (top panels), these losses can be as high as 90% in some channels. This can alter the line ratios by several tens of percent, an effect already reported in previous studies (e.g., Pety et al. 2013).

Figure 16 (right panel) shows how frequency-dependent, spatial filtering effects can also modify the line FWHM and line centroid of the observed gas components. As illustrated in the int-CLEAN spectrum, negative side lobes can selectively alter different channels (see the negative feature in the spectrum), both reducing the line FWHM and shifting the line peak in comparison with the Feather and SDINT reductions. Data combination is therefore essential not only to recover the total flux in spectral cubes but also to preserve the kinematic information in them. For wider frequency coverage, one should also ensure that the frequency dependence of (u, v) spacing and PB are taken into account.

6.3. Comparison between Data Combination Methods

Inspecting Figure 14 in detail suggests that more elaborate methods, such as SDINT (bottom right panel), may be able to reproduce the original sky brightness distribution (top left panel) even better than Feather. We quantitatively investigate

the performance of the different data combination techniques introduced in Section 3, all of which are available in the script we provide. In Figure 17 (left panel), we show the overall A-par values, as well as the total recovered flux in the images (see also figure caption) obtained by the int-CLEAN, Feather, SDINT, and MACF methods, as applied to the sky model. The FSSC method is not shown but produced results nearly identical to Feather in this test. Feather recovers $\sim 89\%$ of the total flux with a mean accuracy of $A\text{-par} = -0.08$ and an accuracy dispersion of $\sigma(A\text{-par}) = 0.24$. The total flux recovery is improved by the SDINT and MACF methods with total flux values above $\sim 92\%$ with respect to the true sky emission. While both are better than Feather, we notice quantifiable differences between the SDINT and MACF methods. While SDINT shows a smaller dispersion of the A-par values ($\sigma(A\text{-par}) = 0.13$, seen as a narrower distribution in this histogram), MACF shows a better mean A-par value ($A\text{-par} = -0.08$, leading to a more centered distribution). These differences are likely connected to the slightly different responses of these methods to the flux intensity (see Figure 17, right panels). Compared to Feather (and FSSC), both SDINT and MACF maximize the flux recovery in those high-intensity flux bins contributing most of the total sky emission.

6.4. Flux and A-par Power Spectra

Continuing the discussion in Section 5.4, we show in Figures 18 and 19 the intensity and A-par power spectra for the results of our simulated sky model observation obtained by interferometry-only and the different combination methods.

The intensity power spectrum (Figure 18) of all combination methods traces quite closely that of the reference at first glance but with small variations. Between the largest scales sampled by our SPS (vertical dotted-dashed line) and $\log(\text{angular scale}) \sim 0.7$, all results are on or above the reference, with SDINT showing the closest power. Between $\log(\text{angular scale}) \sim 0.7$ and ~ 0.4 , the results are constantly below the reference. Here MACF is closer to the reference. Shortly before reaching the smallest accessible angular scales (vertical dashed line), the results rise again above the reference. In this range, SDINT performs best. Although tracing scales rather than only flux recovery, the results of these SPSs are consistent with the analysis of Figure 17 (right panels).

The A-par map power spectra shown in Figure 19 speak a clearer language because in this type of plot, the deviations from the reference occur in the angular scale range where the instrumental sensitivity is actually missing. All results, with or without data combination and no matter which method is used, are far above the reference and only come close to it at the smallest angular scales (right side of the plot). This is because the reference compared to itself has, of course, an A-par of zero, and the nonzero A-par values in the plot are only caused by the added (Gaussian) noise, which has no

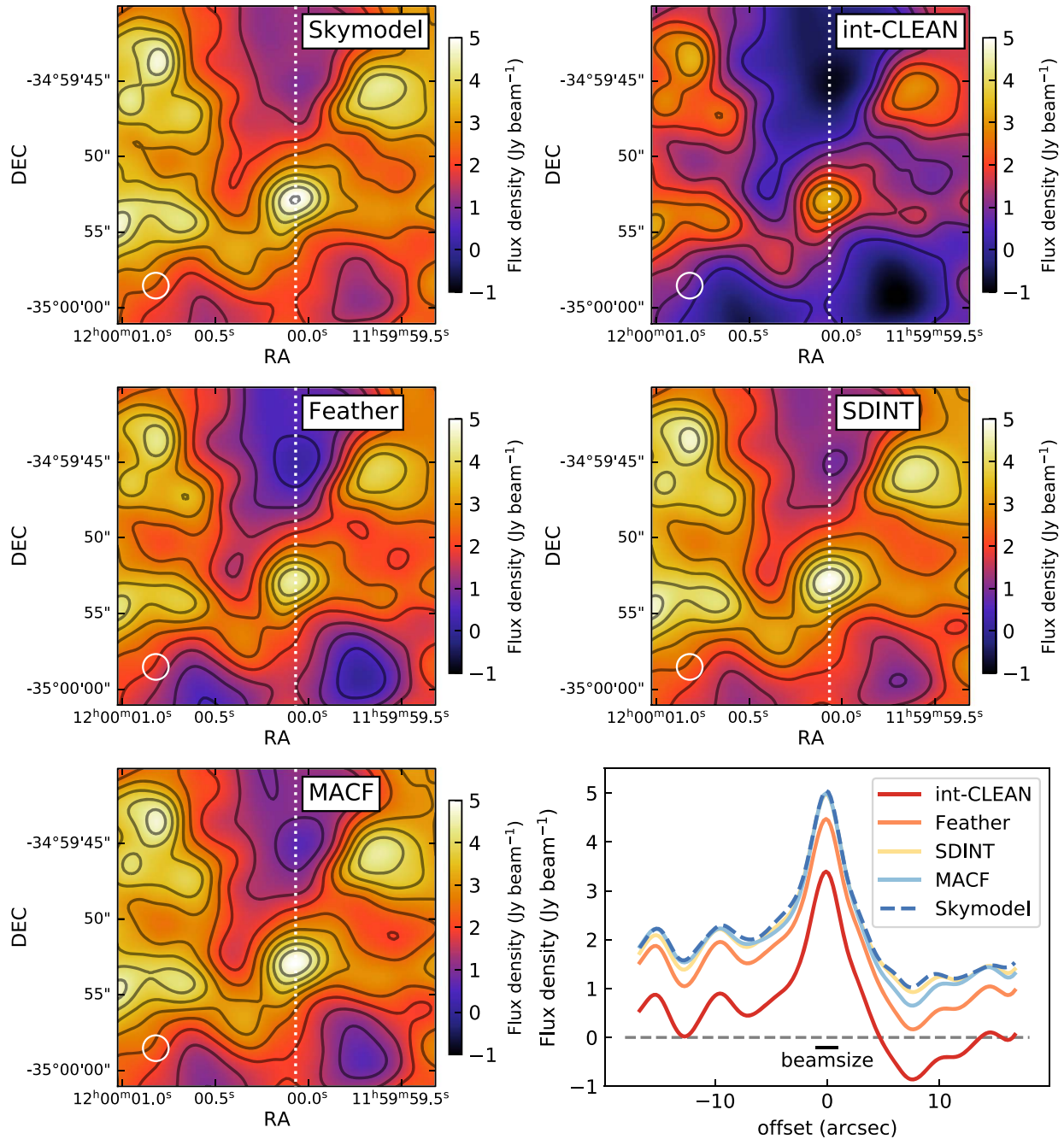


Figure 15. Compact emission recovered by different data combination methods at the central region of the sky model image convolved into a final resolution of $2''$ (see bottom left corner of each image) and plotted within the same intensity range and with the same contours every 0.5 Jy beam^{-1} . From left to right and top to bottom: sky model, int-CLEAN, Feather, SDINT, and MACF results. The bottom right panel shows the intensity profile indicated with a dotted line in our maps obtained by these methods.

spatial structure. The deviations of the reconstructed images from the reference, however, do have a spatial structure, and A-par is extremely sensitive to this (see also Figure 6, lower left panel). In other words, the slopes seen in these A-par SPSs compared to pure white noise (dark blue line)

demonstrate how the deviations of any data combination method compared to the original reference image are not Gaussian but depend on scale and intensity (see the distribution of the A-par variations in Figure 6, lower left panel). With this sensitivity, we can see that SDINT is

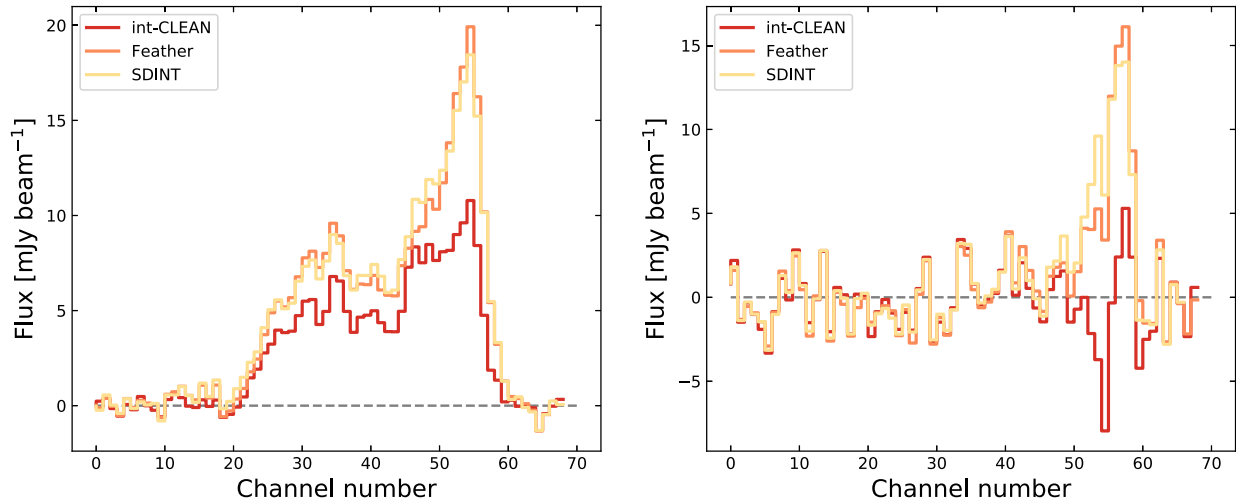


Figure 16. Examples of the data combination on line profiles obtained from our analysis of two representative regions of our M100 data set. In the left panel, the line profile in one region shows effects on the line peaks and relative intensities. In the right panel, the line profile in another, lower-flux region shows effects on the line shape.

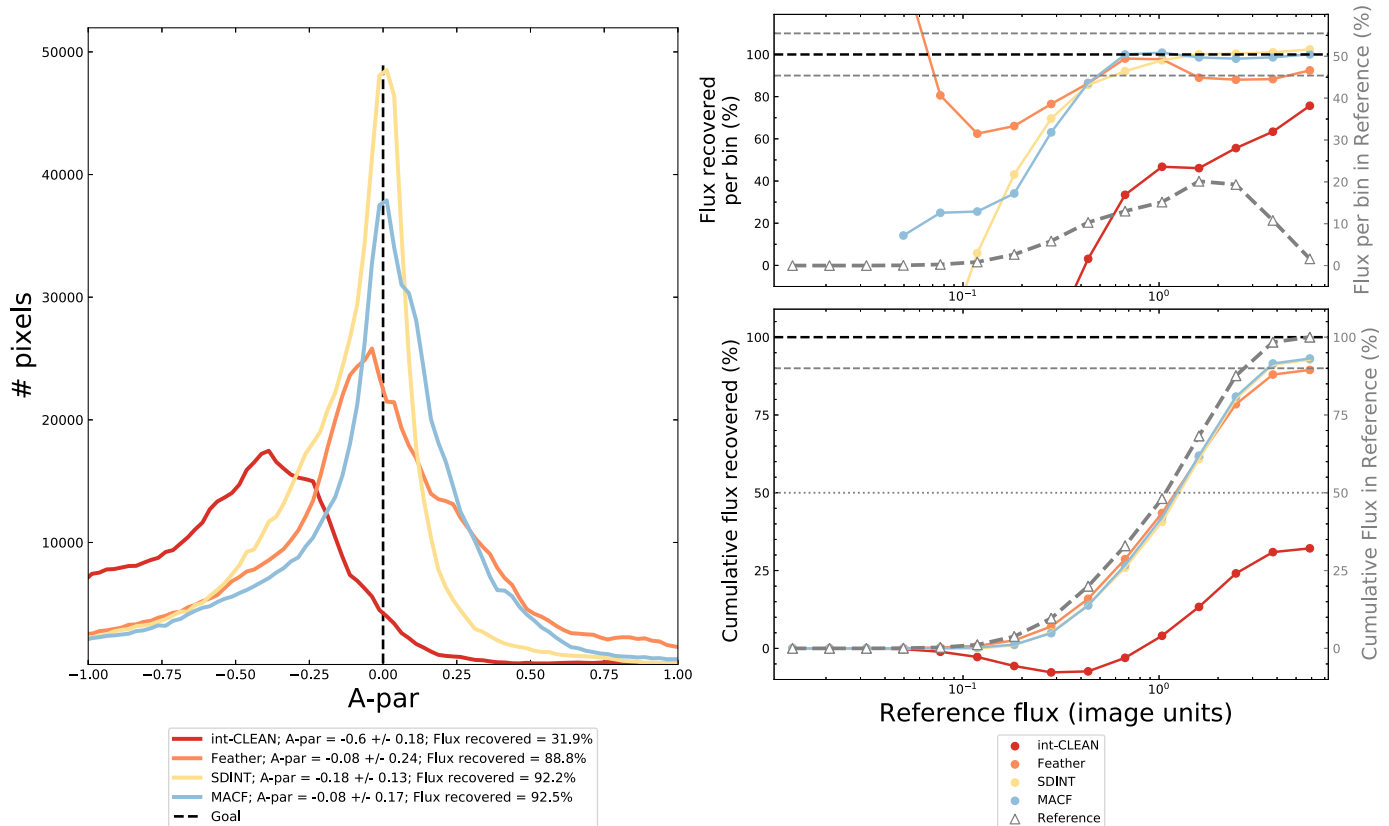


Figure 17. Comparison of the data combination methods for the case of our sky model: int-CLEAN (red), Feather (orange), SDINT (yellow), and MACF (light blue). Left panel: A-par statistics. Right panels: flux recovered by flux bin compared to our sky model as reference (gray triangles). See also Figure 8, as the gray horizontal lines are the same.

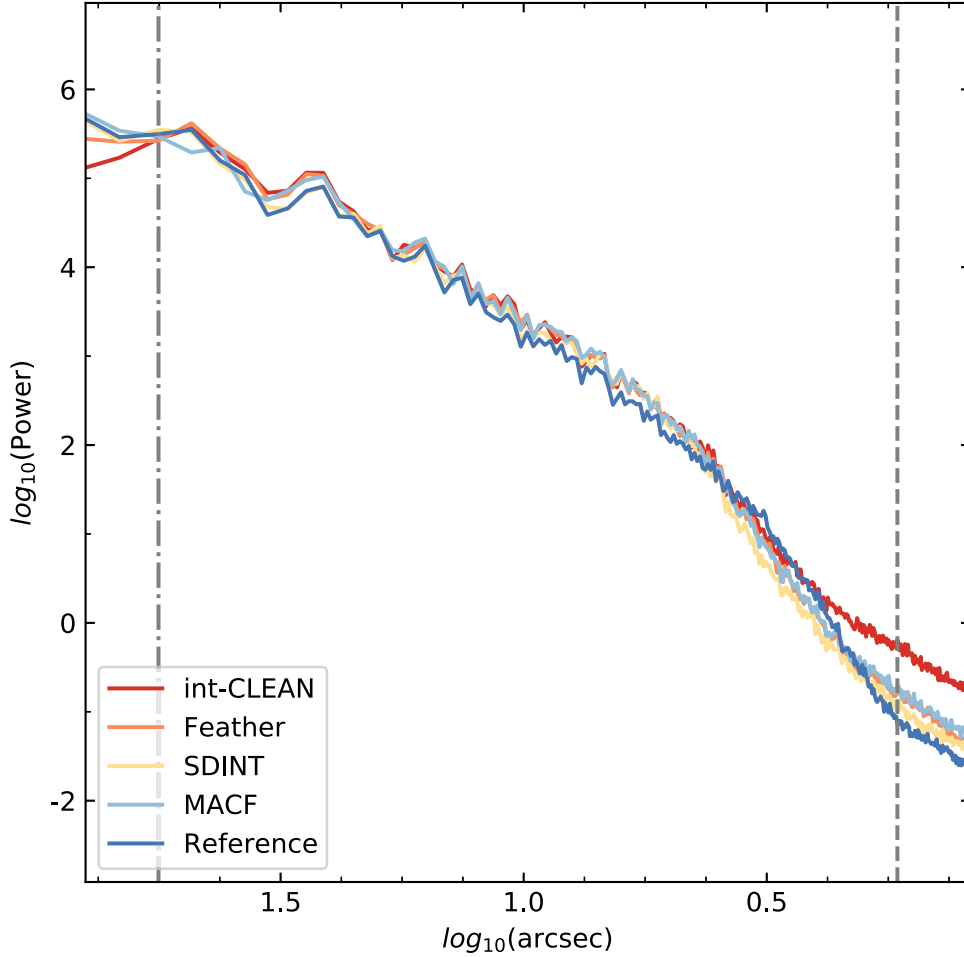


Figure 18. Power spectrum of image intensity as introduced in Section 5.4 and Figure 10, here also showing the results for SDINT (yellow) and MACF (light blue) with our sky model as reference (dark blue). As in Figure 10, vertical lines show the range above and below which this simulated instrument is not sensitive.

performing increasingly better (lower, flatter) than the other combination methods as the angular scale increases (toward the left). This corresponds to the narrowness of the A-par distribution seen in the previous section.

Our experiments demonstrate how interferometers can significantly alter the original power spectrum of a science target, such as that in the sky model. The incomplete sampling of the (u,v) -plane information introduces nonlinear effects at different scales (see the A-par SPS in Figure 18) modifying both the absolute value and slope of the recovered SPS that persist even after data combination (see Figure 19). Similar results are found in other structure analysis techniques, such as probability distribution functions (e.g., see Ossenkopf-Okada et al. 2016). The physical interpretation of the recovered SPS in interferometric observations (e.g., absolute values and changes in the power spectrum slope) should be treated with extreme caution.

6.5. SD Flux Recovery

In Section 5.5, we explained that for actual observational data, the SD image needs to serve as the reference image. Figure 13 already showed the A-par spectrograms for the int-CLEAN image cube and the Feather-combined image cube of our M100 data using the M100 SD image cube as reference. In Figure 20, we show the corresponding plots for the remaining combination methods, SDINT and MACF. Similar to the case of our continuum maps (Section 6.1), all data combination methods produce significant improvements in the image quality of the spectral cube.

In the case of our M100 data set, all methods produce satisfactory results, with deviations from the expected flux per channel reduced to $\lesssim 10\%$ in all cases. The best results are produced by the Feather and MACF methods, both showing narrow A-par distributions ($\sigma(\text{A-par}) = 0.04$) with an average flux recovery of $\gtrsim 95\%$ ($|\text{A-par}| < 0.05$), while SDINT shows

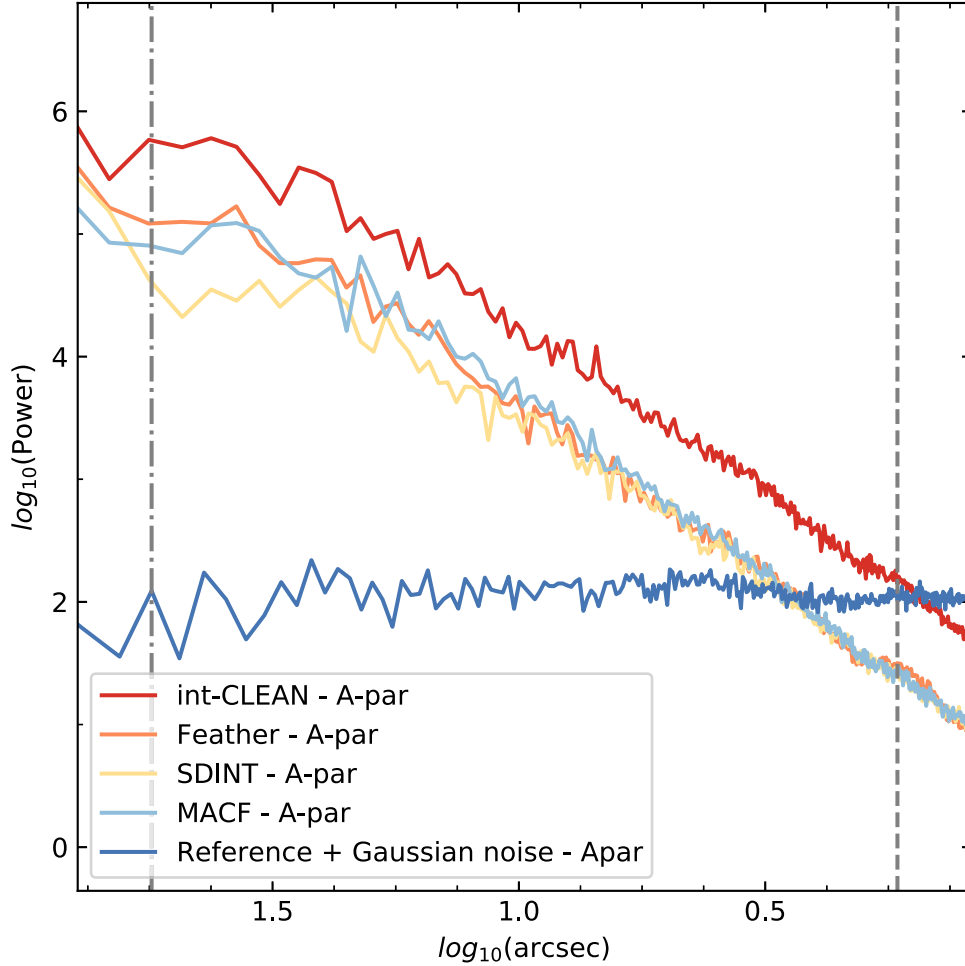


Figure 19. Power spectrum of the A-par map as introduced in Section 5.4 and Figure 11, here also showing the results for SDINT (yellow) and MACF (light blue).

slightly larger differences with respect to the SD flux ($|A\text{-par}| = -0.11$ and $\sigma(A\text{-par}) = 0.06$). Comparisons within these 10% variations are, however, difficult to interpret given the low number statistics available (~ 20 voxels channel^{-1} within the assessment mask) once these analyses are carried out at the SD resolution.

Compared with the results obtained on our sky model, where SDINT and MACF produced the best reductions (Section 6.3), our analysis suggests that the performance of each combination method may slightly vary depending on the spatial structure of the astronomical target, which may vary between velocity channels; there may be additional dependence on the depth and type of observation. While our analysis does not allow us to establish the clear superiority of any of the data combination methods in all situations, our assessment metrics appear to be a useful diagnostic toolkit to systematically investigate and compare their performance, statistically quantify their ability to recover the true sky emission at different scales, and identify potential combination issues in both the continuum and spectral

data sets. For simplicity, our data combinations assumed standard values for reduction parameters such as `briggs` (CLEAN), `sdfactor` (Feather and MACF), and `sdgain` (SDINT), among others (see Sections 2 and 3). The assessments presented here can also be extended to quantify the effect and sensitivity of the flux and scales recovered by other parameter choices and techniques. Users of these methods are therefore recommended to evaluate their results using these diagnostics.

7. Summary

In this paper, we underline with synthetic and real-world examples the importance of the combination of single-dish (SD) data with interferometric data in radio astronomy when the objects observed emit on scales that are larger than a few times the angular resolution of the interferometric observation. We then briefly describe the prominent data combination methods available today (Feather, TP2VIS, MACF, SDINT,

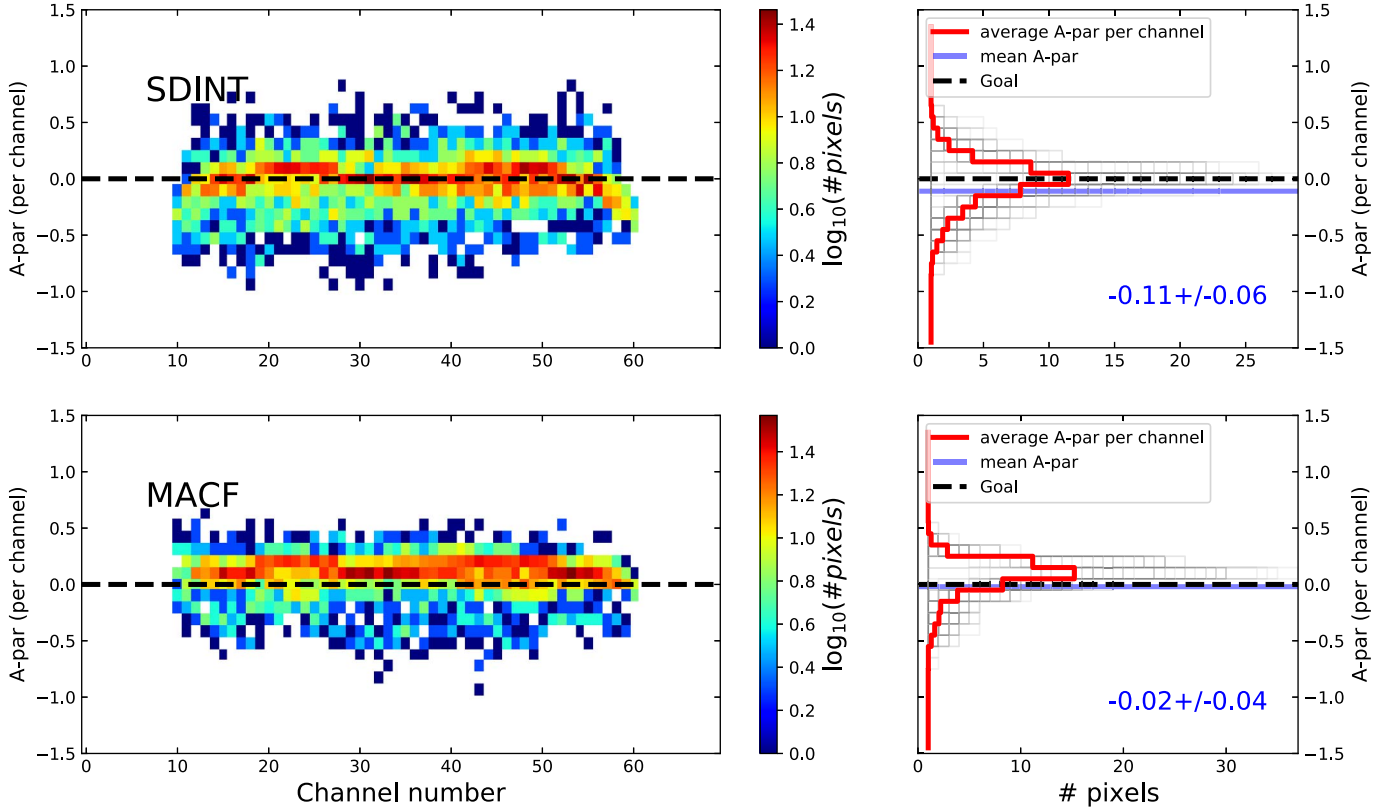


Figure 20. The A-par spectrograms for the SDINT (upper panels) and MACF (lower panels) methods for the case of M100. See also Figure 13.

and FSSC) and test them on two data sets, one simulated and one observational, with a new set of tools producing several novel diagnostic plots that permit one to quantify and compare the performance of the combination methods. These tools are mostly based on the accuracy parameter, A-par, which is essentially the relative difference between the output image of the method and the original input image of the simulation (in the case of simulated test data) or the original SD image (in the case of a real observation). We also discuss the commonly used fidelity parameter, and we find A-par to have higher diagnostic value. An additional valuable diagnostic (closely related to A-par) is the fraction of recovered flux as a function of reference flux either per reference flux bin or cumulative.

For a given observation, A-par can be inspected in four different ways: as a spatial map, as a histogram of the A-par value for all pixels, as a power spectrum of the A-par map (as a function of angular scale), and for spectrally resolved data (image cubes) as a spectrogram that shows the per-channel A-par histograms for each channel next to each other. For individual images (a single spectral channel), the A-par maps and histograms can clearly reveal the need for data combination. For spectrally resolved data, we demonstrate that not applying data combination can result in significantly deformed

spectral line shapes and intensity ratios, and this is clearly visible in the A-par spectrograms.

As a result of our analysis, we recommend obtaining additional SD observations for all interferometric observations of significantly resolved objects amidst extended emission and producing diagnostic A-par plots in order to verify (a) whether combination with SD data is required and (b) whether the combination was performed optimally.

Our results on the performance of the tested data combination methods show quantitatively that the application of any method is better than using the interferometric data on their own. Interferometric-only reductions can miss up to 90% (A-par = -0.9) of the flux depending on the scale and source morphology. These flux losses are present at all scales, affecting both the diffuse emission and compact sources down to scales similar to the beam size. In contrast, the use of data combination techniques such as Feather, SDINT, or MACF allows the recovery of most of the true sky emission within errors of $\lesssim 10\%$ ($|A\text{-par}| < 0.1$). Our tests show that the enhanced performance of some of these methods under certain circumstances can reduce the mean value ($|A\text{-par}| < 0.05$) and variance ($\sigma(A\text{-par}) < 0.05$) of these differences to $< 5\%$ with respect to the actual target flux.

All combination methods have a parameter that permits tuning the contribution of the SD data, the choice of which depends on the relative sensitivity achieved in the interferometric and SD observations. While this parameter should be chosen on first principles, one can also tune the relative weighting of the input data depending on their sensitivities and the scientific goal of the experiment. Moreover, the goodness of these different combinations can be further quantified with our assessment diagnostics.

Recovering the true sky emission at all scales has fundamental implications for the physical interpretation of scientific images. For instance, the continuum flux is directly connected to measurements of the (gas and dust) column densities, probability distribution functions, spectral indices, and masses. Similarly, the line emission profiles provide information on the gas excitation conditions, molecular abundances, and gas chemistry, among others. The addition of the zero-spacing information is revealed as fundamental to produce accurate, high dynamic range images in radio-astronomical, interferometric observations of spatially resolved targets with complex emission substructure. Our results demonstrate the importance of implementing advanced data combination techniques in current (e.g., NOEMA, SMA, and ALMA) and future (e.g., ngVLA and SKA) interferometric studies. The reader is encouraged to try our demonstration software package available from <https://github.com/teuben/DataComb>.






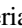






The authors gratefully acknowledge the thorough review and constructive comments from the very knowledgeable anonymous referee. The authors acknowledge the Lorentz Center, which enabled the launch of this initiative through funding, organizing, and hosting the workshop “Improving Image Fidelity on Astronomical Data: Radio Interferometer and Single-Dish Data Combination,” held on 2019 August 12–16. The European Southern Observatory provided additional support. We particularly thank Haiyu Liu, Yanett Contreras, and Alvaro Sanchez-Monge for co-organizing this 2019 Lorentz Center workshop. Including and in addition to participants of the Lorentz Center workshop, we acknowledge in particular Amanda Kepley, Urvashi Rau, Sandra Burkutean, Adam Ginsburg, and Jens Kauffmann, who contributed to the development and discussion of the techniques used in this manuscript. This paper makes use of the following ALMA data: ADS/JAO.ALMA#2011.0.00004.SV. ALMA is a partnership of ESO (representing its member states), NSF (USA) and NINS (Japan), together with NRC (Canada), MOST and ASIAA (Taiwan), and KASI (Republic of Korea), in cooperation with the Republic of Chile. The Joint ALMA Observatory is operated by ESO, AUI/NRAO and NAOJ. The National Radio Astronomy Observatory is a facility of the National

Science Foundation operated under cooperative agreement by Associated Universities, Inc. A.H. and S.S. acknowledge support and funding from the European Research Council (ERC) under the European Union’s Horizon 2020 research and innovation program (grant agreement No. 851435). A.H. acknowledges assistance from Allegro, the European ALMA Regional Center node in the Netherlands. L.M.F. acknowledges funding by the German Federal Ministry of Education and Research under funding code 05A20PD1. Y.M. acknowledges support from grant JSPS KAKENHI (grant No. JP20K04034). K.M.H. acknowledges financial support from grant SEV-2017-0709 funded by MCIN/AEI/10.13039/501100011033, the coordination of the participation in SKA-SPAIN, funded by the Ministry of Science and Innovation (MCIN), and financial support from grants RTI2018-096228-B-C31 and PID2021-123930OB-C21 funded by MCIN/AEI/10.13039/501100011033 by “ERDF A way of making Europe” and by the European Union. This research made use of Astropy (<http://www.astropy.org>), a community-developed core Python package for astronomy (Astropy Collaboration et al. 2013, 2018).

Facility: ALMA.

Software: CASA (The CASA Team et al. 2022), astropy (Astropy Collaboration et al. 2013, 2018), numpy (Harris et al. 2020), scipy (Virtanen et al. 2020), matplotlib (Hunter 2007), analysisUtils (https://casaguides.nrao.edu/index.php/Analysis_Uilities).

ORCID iDs

Adele Plunkett  <https://orcid.org/0000-0002-9912-5705>
 Alvaro Hacar  <https://orcid.org/0000-0001-5397-6961>
 Dirk Petry  <https://orcid.org/0000-0002-8704-7690>
 Peter Teuben  <https://orcid.org/0000-0003-1774-3436>
 Nickolas Pingel  <https://orcid.org/0000-0001-9504-7386>
 Devaky Kunneriath  <https://orcid.org/0000-0002-1568-579X>
 Yusuke Miyamoto  <https://orcid.org/0000-0002-7616-7427>
 Emily Moravec  <https://orcid.org/0000-0001-9793-5416>
 Sümeyye Suri  <https://orcid.org/0000-0003-0412-8522>
 Kelley M. Hess  <https://orcid.org/0000-0001-9662-9089>
 Melissa Hoffman  <https://orcid.org/0000-0003-2523-4631>
 Brian Mason  <https://orcid.org/0000-0002-8472-836X>

References

- Arras, P., Perley, R. A., Bester, H. L., et al. 2021, *A&A*, **646**, A84
 Astropy Collaboration, Price-Whelan, A. M., Sipőcz, B. M., et al. 2018, *AJ*, **156**, 123
 Astropy Collaboration, Robitaille, T. P., Tollerud, E. J., et al. 2013, *A&A*, **558**, A33
 Beuther, H., Wyrowski, F., Menten, K. M., et al. 2022, *A&A*, **665**, A63
 Briggs, D. S. 1995, PhD thesis, New Mexico Institute of Mining and Technology
 Carrillo, R. E., McEwen, J. D., & Wiaux, Y. 2014, *MNRAS*, **439**, 3591
 Clark, B. G. 1980, *A&A*, **89**, 377

- Condon, J. J., Cotton, W. D., Greisen, E. W., et al. 1998, *AJ*, **115**, 1693
- Cornwell, T. J. 2008, *ISTSP*, **2**, 793
- Cornwell, T. J., Holdaway, M. A., & Uson, J. M. 1993, *A&A*, **271**, 697
- Cotton, W. D. 2017, *PASP*, **129**, 094501
- Dirienzo, W. J., Brogan, C., Indebetouw, R., et al. 2015, *AJ*, **150**, 159
- Faridani, S., Bigiel, F., Flöer, L., Kerp, J., & Stanimirović, S. 2018, *AN*, **339**, 87
- Gildas, T. 2013, GILDAS: Grenoble Image and Line Data Analysis Software, Astrophysics Source Code Library, ascl:1305.010
- Hacar, A., Tafalla, M., Forbrich, J., et al. 2018, *A&A*, **610**, A77
- Harris, C. R., Millman, K. J., van der Walt, S. J., et al. 2020, *Natur*, **585**, 357
- Högbom, J. A. 1974, *A&As*, **15**, 417
- Hunter, J. D. 2007, *CSE*, **9**, 90
- Jiao, S., Lin, Y., Shui, X., et al. 2022, *SCPMA*, **65**, 299511
- Jorsater, S., & van Moorsel, G. A. 1995, *AJ*, **110**, 2037
- Kauffmann, J., Pillai, T., Zhang, Q., et al. 2017, *A&A*, **603**, A89
- Kepley, A. A., Tsutsumi, T., Brogan, C. L., et al. 2020, *PASP*, **132**, 024505
- Koda, J., Sawada, T., Wright, M. C. H., et al. 2011, *ApJS*, **193**, 19
- Koda, J., Teuben, P., Sawada, T., Plunkett, A., & Fomalont, E. 2019, *PASP*, **131**, 054505
- Kong, S., Arce, H. G., Feddersen, J. R., et al. 2018, *ApJS*, **236**, 25
- Kurono, Y., Morita, K. -I., & Kamazaki, T. 2009, *PASJ*, **61**, 873
- Leroy, A. K., Schinnerer, E., Hughes, A., et al. 2021, *ApJS*, **257**, 43
- Mason, B. 2021, NGVLA Memo, 67
- Mason, B. S. 2020, arXiv:2006.06549
- Offringa, A. R., McKinley, B., Hurley-Walker, N., et al. 2014, *MNRAS*, **444**, 606
- Ossenkopf-Okada, V., Csengeri, T., Schneider, N., Federrath, C., & Klessen, R. S. 2016, *A&A*, **590**, A104
- Peretto, N., Fuller, G. A., Duarte-Cabral, A., et al. 2013, *A&A*, **555**, A112
- Pety, J. 2005, in SF2A-2005: Semaine de l'Astrophysique Française, ed. F. Casoli et al. (Les Ulis: EdP-Sciences), 721
- Pety, J., & Rodríguez-Fernández, N. 2010, *A&A*, **517**, A12
- Pety, J., Schinnerer, E., Leroy, A. K., et al. 2013, *ApJ*, **779**, 43
- Pineda, J. E., Goodman, A. A., Arce, H. G., et al. 2011, *ApJL*, **739**, L2
- Pingel, N. M., Dempsey, J., McClure-Griffiths, N. M., et al. 2022, *PASA*, **39**, e005
- Plunkett, A. L., Arce, H. G., Corder, S. A., et al. 2013, *ApJ*, **774**, 22
- Plunkett, A. L., Arce, H. G., Corder, S. A., et al. 2015, *ApJ*, **803**, 22
- Rau, U., & Cornwell, T. J. 2011, *A&A*, **532**, A71
- Rau, U., Naik, N., & Braun, T. 2019, *AJ*, **158**, 3
- Remijan, A., Biggs, A., Cortes, P., et al. 2019, ALMA Technical Handbook Cycle 7 (ALMA Doc. 7.3, v1.1)
- Rodríguez-Fernández, N. J., Pety, J., & Gueth, F. 2008, Single-dish observation and processing to produce the short-spacing information for a millimeter interferometer, Tech. Rep., IRAM, Grenoble
- Sault, R. J., Teuben, P. J., & Wright, M. C. H. 1995, in ASP Conf. Ser. 77, Astronomical Data Analysis Software and Systems IV, ed. R. A. Shaw, H. E. Payne, & J. J. E. Hayes (San Francisco, CA: ASP) arXiv:astro-ph/0612759
- Stanimirovic, S. 2002, in ASP Conf. Ser. 278, Single-Dish Radio Astronomy: Techniques and Applications, ed. S. Stanimirovic et al. (San Francisco, CA: ASP) 375–96 arXiv:astro-ph/0205329
- Tang, Y., Wang, Q. D., & Wilson, G. W. 2021a, *MNRAS*, **505**, 2377
- Tang, Y., Wang, Q. D., Wilson, G. W., et al. 2021b, *MNRAS*, **505**, 2392
- The CASA Team, Bean, B., Bhatnagar, S., et al. 2022, *PASP*, **134**, 114501
- van Moorsel, G., Kemball, A., & Greisen, E. 1996, in ASP Conf. Ser. 101, Astronomical Data Analysis Software and Systems V, ed. G. H. Jacoby & J. Barnes (San Francisco, CA: ASP), 37
- Virtanen, P., Gommers, R., Oliphant, T. E., et al. 2020, *NatMe*, **17**, 261
- Wang, Y., Beuther, H., Rugel, M. R., et al. 2020, *A&A*, **634**, A83
- Williams, G. M., Peretto, N., Avison, A., Duarte-Cabral, A., & Fuller, G. A. 2018, *A&A*, **613**, A11
- Wilner, D. J., & Welch, W. J. 1994, *ApJ*, **427**, 898